© 2020. Published by The Company of Biologists Ltd | Development (2020) 147, dev189076. doi:10.1242/dev.189076

RESEARCH ARTICLE

The hedgehog co-receptor BOC differentially regulates SHH signaling during craniofacial development

Martha L. Echevarría-Andino* and Benjamin L. Allen*

ABSTRACT

The Hedgehog (HH) pathway controls multiple aspects of craniofacial development. HH ligands signal through the canonical receptor PTCH1, and three co-receptors: GAS1, CDON and BOC. Together, these co-receptors are required during embryogenesis to mediate proper HH signaling. Here, we investigated the individual and combined contributions of GAS1, CDON and BOC to HH-dependent mammalian craniofacial development. Notably, individual deletion of either *Gas1* or *Cdon* results in variable holoprosencephaly phenotypes in mice, even on a congenic background. In contrast, we find that *Boc* deletion results in facial widening that correlates with increased HH target gene expression. In addition, *Boc* deletion in a *Gas1* null background partially ameliorates the craniofacial defects observed in *Gas1* single mutants; a phenotype that persists over developmental time, resulting in significant improvements to a subset of craniofacial structures. This contrasts with HH-dependent phenotypes in other tissues that significantly worsen following combined deletion of *Gas1* and *Boc*. Together, these data indicate that BOC acts as a multi-functional regulator of HH signaling during craniofacial development, alternately promoting or restraining HH pathway activity in a tissue-specific fashion.

KEY WORDS: Hedgehog, GAS1, CDON, BOC, Craniofacial development, Holoprosencephaly, Mouse

INTRODUCTION

Hedgehog (HH) signaling regulates the patterning and growth of nearly every tissue in the body (Briscoe and Thérond, 2013; McMahon et al., 2003). Aberrant HH pathway activity results in severe birth defects including holoprosencephaly (HPE), a defect characterized by the failure of the division of the embryonic forebrain into two cerebral hemispheres (Muenke and Beachy, 2000). HPE is one of the most common birth defects in humans, estimated to affect as many as 1 in 250 embryos (Hong and Krauss, 2018). The clinical manifestations of HPE are highly heterogeneous, consisting of a wide phenotypic spectrum of defects (Schachter and Krauss, 2008). Notably, 80% or more of HPE cases will display facial defects in addition to the forebrain malformations (Schachter and Krauss, 2008).

Multiple mutations associated with developmental signaling pathways such as HH have been identified in human HPE patients (Roessler and Muenke, 2010). Specifically, mutations in sonic hedgehog (*SHH*) account for 6%-8% of sporadic HPE (Roessler et al., 2009). During craniofacial development, *Shh* regulates the establishment of forebrain identity and patterns the face primordia (Schachter and Krauss, 2008). Moreover, disruption of *Shh* in mice results in abnormal dorsoventral patterning in the neural tube, defective axial skeleton formation and alobar HPE (Chiang et al., 1996).

SHH ligands signal through the twelve-pass transmembrane receptor patched 1 (PTCH1) (Marigo et al., 1996). However, SHH also binds three co-receptors, growth arrest-specific 1 (GAS1), CAM-related/downregulated by oncogenes (CDON) and brother of CDON (BOC) (Allen et al., 2011, 2007; Beachy et al., 2010; Izzi et al., 2011; Lee et al., 2001; McLellan et al., 2008; Tenzen et al., 2006; Yao et al., 2006; Zhang et al., 2011, 2006). CDON and BOC are structurally similar members of the immunoglobulin superfamily that are conserved from *Drosophila* to mammals (Beachy et al., 2010; Kang et al., 1997, 2002; Lum et al., 2003). GAS1 is a vertebrate-specific GPI-anchored protein with structural resemblance to GDNF receptors (Cabrera et al., 2006). In the absence of SHH ligand, PTCH1 inhibits the activity of the GPCR-like protein smoothened (SMO). SHH ligand binding to PTCH1 and GAS1, CDON or BOC releases SMO inhibition leading to a signal transduction cascade that leads to modulation of the GLI family of transcriptional effectors (Hui and Angers, 2011). Together, GAS1, CDON and BOC are required for HH signal transduction during embryogenesis (Allen et al., 2011, 2007; Cole and Krauss, 2003; Izzi et al., 2011; Martinelli and Fan, 2007; Tenzen et al., 2006; Zhang et al., 2011, 2006).

Similar to *Shh* mutants, simultaneous genetic removal of *Gas1*, *Cdon* and *Boc* results in alobar HPE (Allen et al., 2011). Further, multiple mutations in these HH co-receptors have been identified in human HPE patients (Bae et al., 2011; Hong et al., 2017; Ribeiro et al., 2010), suggesting that these proteins play key roles in craniofacial development. This is supported by multiple studies in mice demonstrating a role for these genes during HH-dependent craniofacial development (Cole and Krauss, 2003; Seppala et al., 2007, 2014; Zhang et al., 2011, 2006). *Gas1* and *Cdon* single mutants display microforms of HPE, in which the severity of the phenotype is dependent on the genetic background of the mouse model (Allen et al., 2007; Cole and Krauss, 2003; Seppala et al., 2007; Zhang et al., 2006). In contrast, in mixed genetic backgrounds *Boc* deletion does not result in any HPE phenotypes, although these animals do display defects in SHH-dependent commissural axon guidance (Okada et al., 2006; Seppala et al., 2014; Zhang et al., 2011). More recently, *Boc* has been demonstrated to function as a silent HPE modifier gene that, in the context of other HPE mutations, can modify the severity of the HPE phenotype (Hong and Krauss, 2018). It has been proposed that modifier genes such as *Boc* contribute to the phenotypic differences observed in different genetic backgrounds.

GAS1, CDON and BOC have generally been described as positive regulators of the HH signaling pathway. However, in

Department of Cell and Developmental Biology, University of Michigan, Ann Arbor, MI 48109, USA.

*Authors for correspondence (mechevar@umich.edu, benallen@umich.edu)

B.L.A., 0000-0003-2323-8313

Handling Editor: James Briscoe
Received 4 February 2020; Accepted 6 October 2020

Development (2020) 147, dev189076. doi:10.1242/dev.189076

certain contexts these co-receptors can act to restrain HH signaling. For example, *Gas1* can antagonize HH signaling in presomitic mesoderm explants (Lee et al., 2001), and restricts HH signaling during tooth development in mice (Cobourne et al., 2004; Ohazama et al., 2009). Similarly, *Cdon* negatively regulates HH pathway function in the optic vesicle of zebrafish and chick embryos (Cardozo et al., 2014). It remains unclear how these co-receptors differentially regulate HH signaling in these different contexts.

Here, we investigated the contributions of GAS1, CDON and BOC to HH-dependent mammalian craniofacial development. Specifically, we examined the individual and combined deletion of different HH co-receptors on a congenic C57BL/6J background. Surprisingly, we found that *Boc* mutants display facial widening and increased HH target gene expression in the nasal processes. In addition, deletion of *Boc* in a *Gas1* null background partially ameliorates the craniofacial defects observed in *Gas1* single mutants, whereas other HH-dependent phenotypes in these mutants significantly worsened. Interestingly, the rescue of the craniofacial defects in *Gas1;Boc* mutants persists over developmental time, but is restricted to the nostrils and the soft tissues of the craniofacial structures. Finally, we provide evidence that BOC selectively restricts neural crest-derived mesenchymal proliferation. Together, our data indicate that BOC acts as a multi-functional regulator of HH signaling during craniofacial development, alternately promoting or restraining HH pathway activity in a tissue-specific fashion.

RESULTS

To define the expression of the HH pathway co-receptors *Gas1*, *Cdon* and *Boc* during early craniofacial development, we used *lacZ* (*Gas1* and *Cdon*) and *alkaline phosphatase* (*AP*; *Boc*) reporter alleles (Fig. 1) (Cole and Krauss, 2003; Martinelli and Fan, 2007; Zhang et al., 2011). At embryonic day (E) 8.5 *Gas1*, *Cdon* and *Boc* are primarily expressed in the cranial neural folds, the somites and the neural tube (Fig. 1A-D). During this stage, *Cdon* is the only co-receptor expressed in the prechordal plate (PCP; see arrowhead in Fig. 1C inset), a major signaling center during craniofacial development that secretes SHH ligand, which patterns the ventral forebrain (Cordero et al., 2004; Rubenstein and Beachy, 1998; Zhang et al., 2006). As development progresses, these expression patterns are maintained in the somites and neural tube, and expand to additional structures. At E9.5, the HH co-receptors are all expressed in the frontonasal prominence (FNP), maxillary process (MXP) and mandibular process (MP; Fig. 1E-H). Differences in *Gas1*, *Cdon* and *Boc* expression in craniofacial structures are revealed by analysis of E10.5 embryos (Fig. 1I-T).

En face views of whole-mount stained E10.5 embryos (Fig. 1M-P) demonstrate broad expression of *Gas1*, *Cdon* and *Boc* in the forebrain. X-gal and AP staining in coronal sections of E10.5 embryos reveals that all three co-receptors are present in the surface ectoderm and in the forebrain neuroepithelium (NE) in a dorsoventral gradient (Fig. 1Q-T; Fig. S1A-D). Notably, the ventral extent of *Cdon* expression in the NE is greatly restricted compared with *Gas1* and *Boc*. Similarly, *Gas1* and *Boc* display broad expression in the olfactory epithelium (OE), whereas *Cdon* expression is limited to a subset of cells in the medial OE of the lateral nasal process (LNP; see arrowhead in Fig. 1S, Fig. S1G).

At E10.5, *Gas1* is the only co-receptor expressed in the MP and in the MXP (Fig. 1J,N). Further differences in the expression of the HH co-receptors are detected in the medial nasal process (MNP) and LNP. All three co-receptors are expressed in the LNP (Fig. 1Q-T). However, *Gas1* and *Boc* are expressed throughout the LNP mesenchyme, whereas *Cdon* expression is restricted to the most dorsal aspect of the LNP mesenchyme (Fig. 1S, Fig. S1G). In the MNP, *Gas1* and *Boc* are broadly expressed at lower levels in the mesenchyme; in contrast, *Cdon* is only expressed in mesenchymal cells that are proximal to the NE (Fig. 1S, Fig. S1G). The expression of *Gas1*, *Cdon* and *Boc* in the craniofacial structures is consistent with their general negative transcriptional regulation by the HH signaling pathway (Allen et al., 2007; Tenzen et al., 2006). In addition to the differences in expression of the HH co-receptors in craniofacial structures, their expression in other HH-responsive tissues, such as the forelimb bud (Fig. S1J-L) and the neural tube (Fig. S1N-P), is also not identical. In particular, the expression domains of *Boc* in the forebrain NE (Fig. S1H) and in the neural tube (Fig. S1P) extend further ventrally, and closer to the sources of *Shh* expression in these tissues, namely the ventral telencephalon and the notochord/floor plate, respectively. These data raise the question of whether these co-receptors, and BOC in particular, may differentially contribute to HH-dependent craniofacial development.

To address the individual contributions of *Gas1*, *Cdon* and *Boc* to craniofacial development, we examined single mutant embryos at mid-gestation on a congenic C57BL/6J background (Fig. 2A-L). At E10.5, $Gas1^{-/-}$ and $Cdon^{-/-}$ embryos display a spectrum of HPE phenotypes that range from proper telencephalic vesicle (TV) division with normal MNP separation, to no TV division with no MNP separation (Fig. S2). Most of these mutants exhibit incomplete TV division (76% of $Gas1^{-/-}$ embryos and 50% of $Cdon^{-/-}$ embryos), whereas a smaller portion (12% and 17%, respectively) of these mutants fails to divide the TV (Fig. S2H). $Gas1^{-/-}$ and $Cdon^{-/-}$ embryos predominantly show either incomplete MNP separation (47% of $Gas1^{-/-}$ embryos and 33% of $Cdon^{-/-}$ embryos) or no MNP separation (29% and 42%, respectively; Fig. S2I). Notably, a minority of *Gas1* and *Cdon* mutants have more mild phenotypes that are characterized by normal TV division (Fig. S2H) and either normal or reduced MNP separation (Fig. S2I). In contrast, $Boc^{-/-}$ embryos do not manifest any gross craniofacial defects (Fig. 2J-L), with 100% of embryos displaying normal TV division and normal MNP separation (Fig. S2H-I). Together, these data indicate that, even on a congenic C57BL/6J genetic background, there remains a spectrum of HPE phenotypes observed in *Gas1* and *Cdon* mutants. Strikingly, and despite the broad expression of *Boc* in multiple HH-responsive cell types in the developing forebrain (Fig. 1), we do not observe any HPE phenotypes in *Boc* mutants maintained on a C57BL/6J background.

To further characterize the spectrum of HPE phenotypes, we quantified the internasal distance in E10.5 embryos. Consistent with our initial assessment, this quantitation revealed significant reductions in the internasal distance in both *Gas1* and *Cdon* mutant embryos (Fig. 2M). Surprisingly, this quantitation also revealed an unexpected subtle, but significant, increase in the internasal distance in *Boc* mutant embryos compared with wild-type embryos (443µm in wild-type embryos, 496µm in $Boc^{-/-}$ embryos; Fig. 2M). These data suggest potentially opposing roles for *Gas1* and *Cdon* compared with *Boc* during mammalian craniofacial development. One explanation for these counterintuitive results is that the increased internasal distance in *Boc* embryos was due to an overall increase in embryo size. Therefore, we measured the crown-rump length (CRL) in E10.5 wild-type and mutant embryos (Fig. S3A-E). Whereas *Gas1* mutants are significantly smaller than their wild-type littermates, both *Cdon* and *Boc* mutant embryos have similar CRL to wild-type embryos (Fig. S3F). These data support the notion that the MNP widening observed in *Boc* mutants at E10.5

Development (2020) 147, dev189076. doi:10.1242/dev.189076

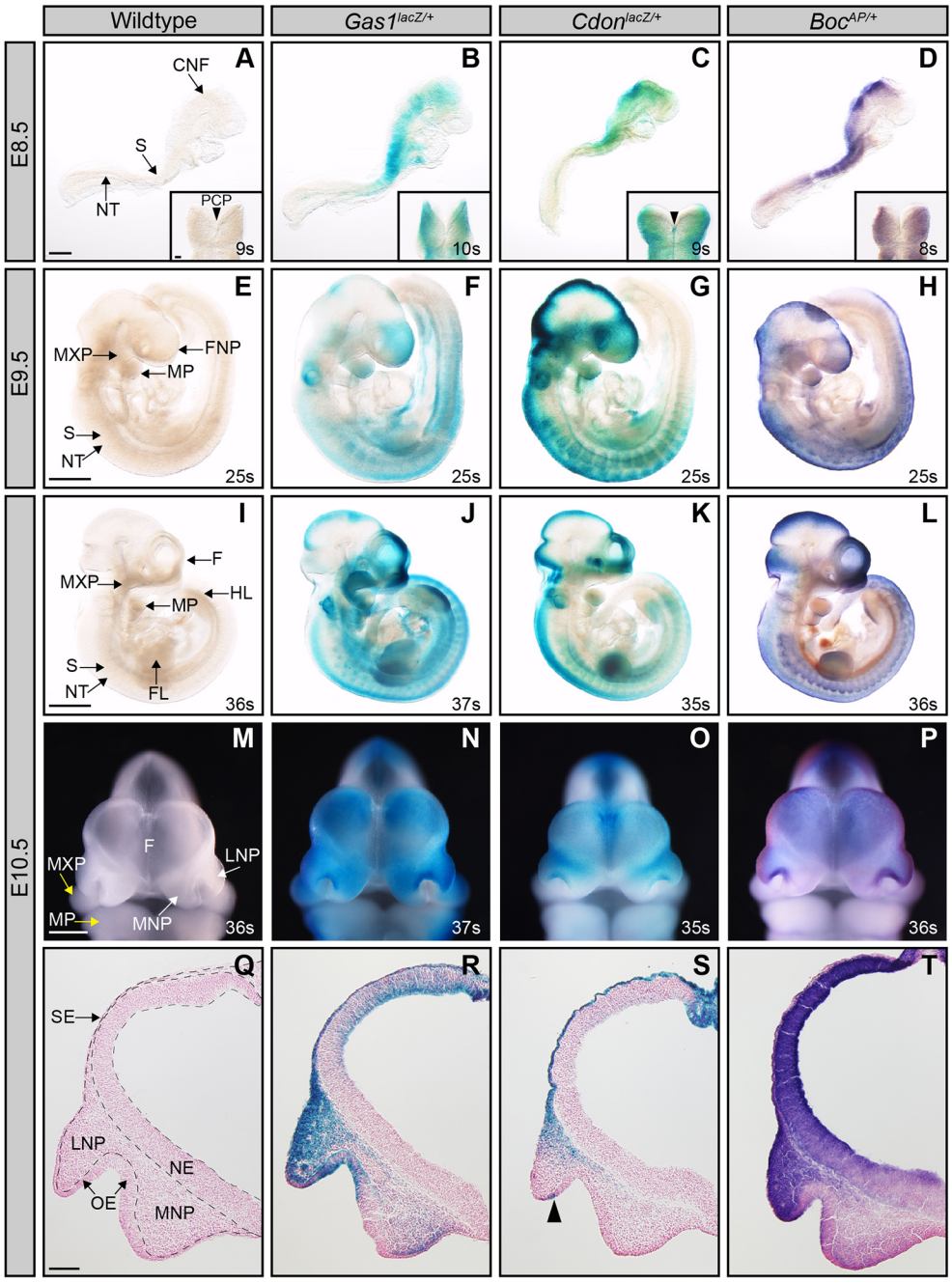

Fig. 1. The HH co-receptors *Gas1*, *Cdon* and *Boc* are expressed throughout early craniofacial development. (A-T) Analysis of HH co-receptor expression using *lacZ* (*Gas1*, *Cdon*) and *hPLAP* (*Boc*) reporter alleles. Whole-mount X-gal and AP staining of E8.5 (A-D), E9.5 (E-H), and E10.5 (I-L), wild-type (A,E,I,M,Q), $Gas1^{lacZ/+}$ (B,F,J,N,R), $Cdon^{lacZ/+}$ (C,G,K,O,S), and $Boc^{AP/+}$ (D,H, L,P,T) embryos is shown. Somite number (s) is indicated in the lower right corner of each panel. Dorsal views of the cranial neural folds of E8.5 embryos are shown in insets (A-D); black arrowheads denote the prechordal plate (PCP). Frontal view of craniofacial structures of E10.5 embryos (M-P). White arrows denote LNP and MNP, and yellow arrows denote MXP and MP (M). Coronal sections of E10.5 forebrains (Q-T); arrowhead (S) denotes a subset of cells expressing *Cdon* in the olfactory epithelium. CNF, cranial neural fold; F, forebrain; FL, forelimb; FNP, frontonasal prominence; HL, hindlimbs; LNP, lateral nasal process; MNP, medial nasal process; MP, mandibular process; MXP, maxillary process; NE, neuroepithelium; NT, neural tube; OE, olfactory epithelium; PCP, pre-chordal plate; S, somite; SE, surface ectoderm. Scale bars: 500 µm (A-P); 50 µm (A-D insets); 200 µm (Q-T insets).

reflects differences in the contribution of this HH co-receptor to craniofacial development. Interestingly, widening or duplication of midfacial tissues is associated with increased levels of HH signaling (Brugmann et al., 2010; Hu and Helms, 1999).

To determine whether the variable craniofacial defects observed in these HH co-receptor mutant embryos correlates with HH pathway activity, we performed *in situ* hybridization for *Gli1*, a general and direct transcriptional target of HH signaling (Dai et al., 1999). *Gli1* is expressed in multiple craniofacial structures, including the MNP, MXP and MP (Fig. S4A). $Gas1^{-/-}$ and $Cdon^{-/-}$ embryos with less severe HPE phenotypes maintain *Gli1* expression in the MNP, but embryos with increasingly severe HPE phenotypes display a loss of *Gli1* expression in the MNP (Fig. S4D-F,G-I). In contrast, in $Boc^{-/-}$ embryos *Gli1* expression is maintained in the MNP across all *Boc* mutant embryos (Fig. S4J-L). To quantify changes in *Gli1* expression we performed qRT-PCR in E11.5 nasal processes (Fig. 2N). $Boc^{-/-}$ embryos display a significant increase in *Gli1* expression, consistent with the internasal distance widening (Fig. 2M). In contrast, and consistent with the *in situ* hybridization data, $Gas1^{-/-}$ embryos display a significant decrease in *Gli1* (Fig. 2N). We also explored whether changes in *Gli1* mRNA translated into protein level differences (Fig. 2O). *Boc* mutants maintain similar levels of GLI1 protein as wild-type embryos, whereas GLI1 protein is reduced in *Gas1* mutants. Although these changes do not reach the level of statistical significance (Fig. S3G), these results are consistent with both the *Gli1 in situ* hybridization and qRT-PCR results. Taken together, these data indicate that HPE severity in *Gas1* and *Cdon* mutant embryos correlates with *Gli1* loss in the nasal processes, and demonstrate that, in contrast to *Gas1* and *Cdon*, *Boc* mutants display increased *Gli1* expression in the nasal

Development (2020) 147, dev189076. doi:10.1242/dev.189076

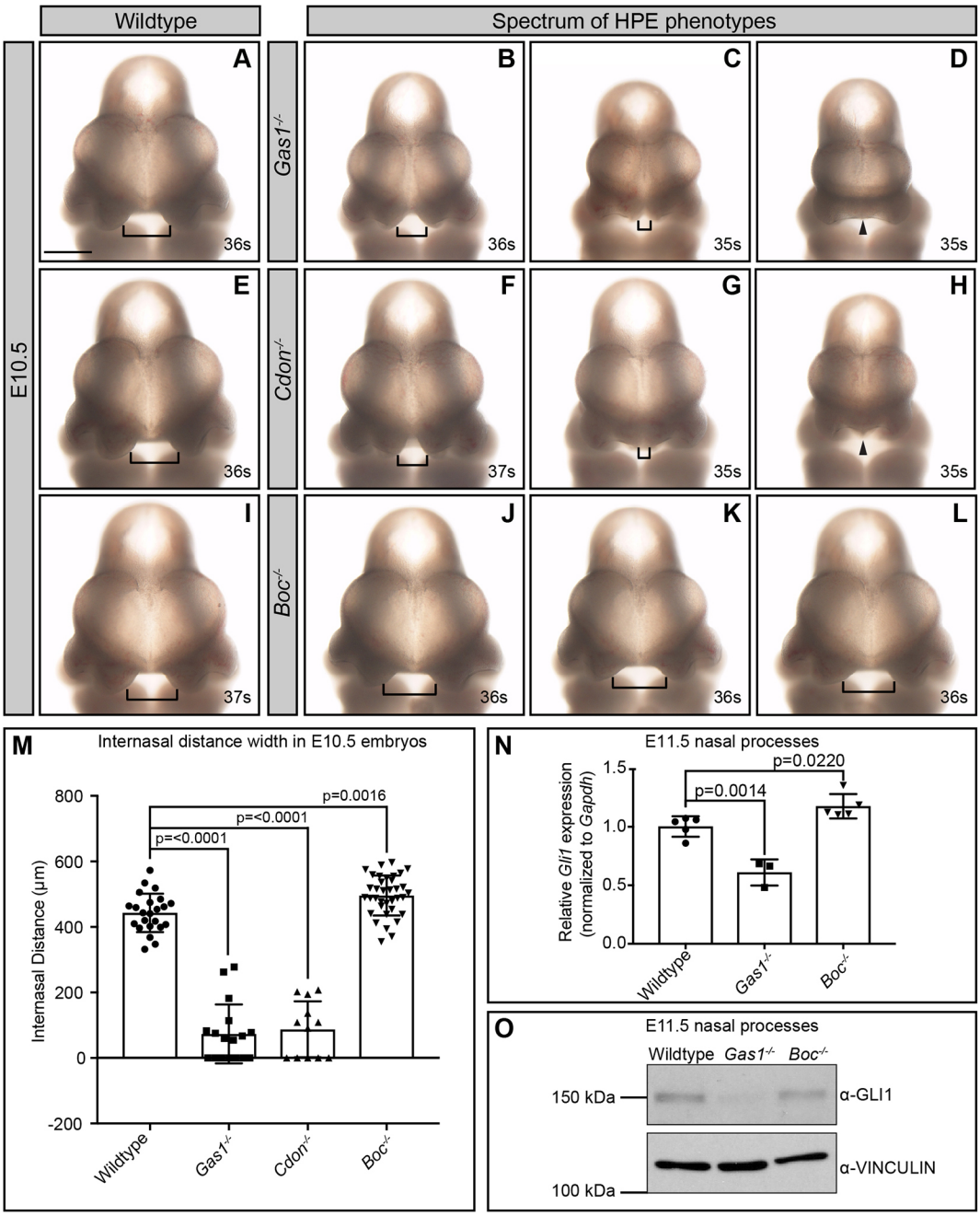

Fig. 2. Loss of *Boc* results in midface widening and increased *Gli1* expression on a congenic C57BL/6J background. (A-L) *En face* view of E10.5 mouse embryos. Somite number (s) is indicated in the lower right corner of each panel. Brackets indicate internasal distance. Black triangles denote fusion of the medial nasal process. E10.5 wild-type (A,E,I), *Gas1*$^{-/-}$ (B-D), *Cdon*$^{-/-}$ (F-H) and *Boc*$^{-/-}$ (J-L) embryos. Note that *Gas1* and *Cdon* mutants display a range of craniofacial defects (increasing in severity from left to right), whereas *Boc* mutants do not display any gross morphological changes. (M) Internasal distance quantitation in wild-type (*n*= 23), *Gas1*$^{-/-}$ (*n*=17), *Cdon*$^{-/-}$ (*n*=12) and *Boc*$^{-/-}$ (*n*=36) embryos. (N) Relative expression of *Gli1* by qRT-PCR in the nasal processes of E11.5 wild-type (*n*=5), *Gas1*$^{-/-}$ (*n*=3) and *Boc*$^{-/-}$ (*n*=5) embryos normalized to *Gapdh*. Biological replicates were analyzed in triplicate. Data are mean±s.d. *P*-values were determined by a two-tailed Student's *t*-test. The Bonferroni correction was employed to account for multiple comparisons in each dataset; (M) not significant ($P>0.0166$), significant ($P\leq0.0166$) and (N) not significant ($P>0.0250$), significant ($P\leq0.0250$). (O) Western blot analysis of endogenous GLI1 protein in the nasal processes from E11.5 wild-type, *Gas1*$^{-/-}$ and *Boc*$^{-/-}$ embryos. Vinculin was used as loading control, three biological replicates were analyzed. Scale bar: 500 µm.

processes. These data suggest an antagonistic role for BOC during HH-dependent craniofacial development.

Previous studies have suggested that combinatorial deletion of *Gas1*, *Cdon* or *Boc* results in more severe HPE phenotypes (Allen et al., 2011, 2007; Seppala et al., 2014; Zhang et al., 2011), suggesting that HH co-receptors positively regulate HH signaling during craniofacial development. In contrast, the midface widening that we observe in *Boc*$^{-/-}$ embryos (Fig. 2M) is consistent with a role for *Boc* as a potential HH antagonist during craniofacial development. To explore this possibility, we deleted *Boc* in combination with *Gas1* deletion on a congenic C57BL/6J background (Fig. 3A-D).

Development (2020) 147, dev189076. doi:10.1242/dev.189076

Analysis of E10.5 *Gas1*$^{-/-}$;*Boc*$^{-/-}$ embryos revealed a spectrum of HPE phenotypes, as observed in *Gas1*$^{-/-}$ embryos (Fig. 3). Importantly, the HPE phenotypes observed in *Gas1;Boc* double mutants are less severe than those observed in *Gas1* single mutants (compare Fig. 3B,D). Specifically, we observed an increase in the percentage of *Gas1;Boc* double mutants with normal TV division compared with *Gas1* single mutants (31% versus 12%, respectively; Fig. 3E). Further, we found that 50% of *Gas1;Boc* double mutants display MNP separation compared with 24% of *Gas1* mutants (Fig. 3F). To investigate whether this rescue was due to increased overall embryo size, we measured the CRL of *Gas1*$^{-/-}$;*Boc*$^{-/-}$ embryos (Fig. S5A-E). We found that *Gas1*$^{-/-}$;*Boc*$^{-/-}$ embryos

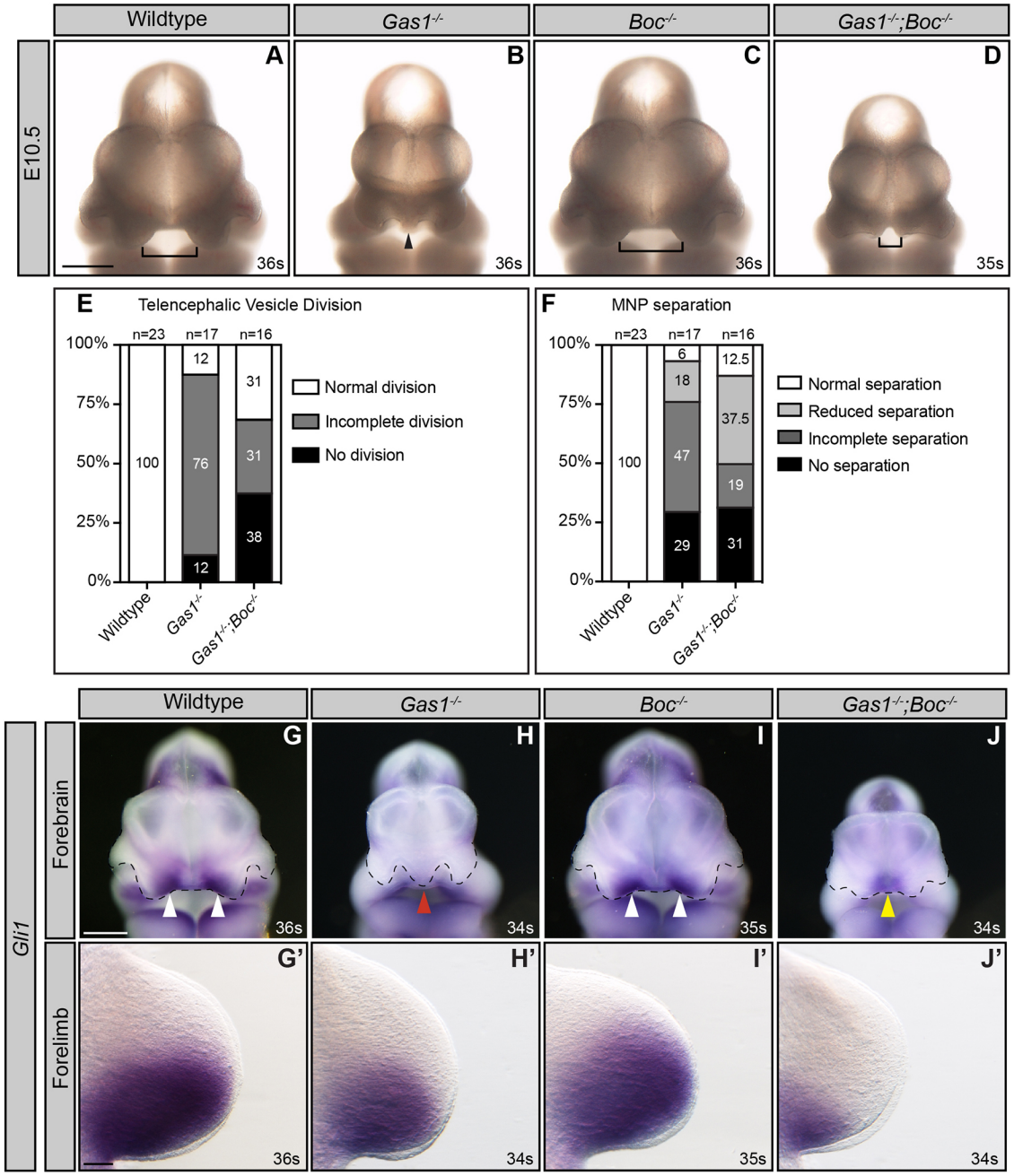

Fig. 3. Tissue-specific rescue of HH signaling in E10.5 *Gas1;Boc* double mutant embryos. (A-D) *En face* view of E10.5 wild-type (A), *Gas1*$^{-/-}$ (B), *Boc*$^{-/-}$ (C) and *Gas1*$^{-/-}$;*Boc*$^{-/-}$ (D) embryos. Brackets indicate internasal distance. Arrowhead denotes fusion of the medial nasal process (MNP). (E) Telencephalic vesicle (TV) division frequency in E10.5 wild-type (*n*=23), *Gas1*$^{-/-}$ (*n*=17) and *Gas1*$^{-/-}$;*Boc*$^{-/-}$ (*n*=16) embryos. TV division was classified according to the following categories: normal division, incomplete division and no division (see Fig. S2A-C for representative examples of each category). (F) MNP separation frequency in E10.5 wild-type (*n*=23), *Gas1*$^{-/-}$ (*n*=17) and *Gas1*$^{-/-}$;*Boc*$^{-/-}$ (*n*=16) embryos. MNP separation in each embryo was classified according to the following categories: normal separation, reduced separation, incomplete separation and no separation (see Fig. S2D-G for representative examples of each category). (G-J′) *In situ* hybridization detection of *Gli1* expression in E10.5 forebrains (G-J) and their corresponding forelimbs (G′-J′). *En face* view of E10.5 forebrains and dorsal view of E10.5 forelimbs in wild-type (G,G′), *Gas1*$^{-/-}$ (H,H′), *Boc*$^{-/-}$ (I,I′) and *Gas1*$^{-/-}$;*Boc*$^{-/-}$ (J,J′) embryos. Black dotted lines outline nasal processes. Note that *Gli1* is differentially regulated in the MNP and forelimb of *Gas1;Boc* mutants. Somite number (s) is indicated in the lower right corner of each panel. Scale bar: 500 µm in A and G; 100 µm in G′.

Development (2020) 147, dev189076. doi:10.1242/dev.189076

tended to be smaller than *Gas1*$^{-/-}$ embryos (Fig. S5F); although not statistically significant, these data rule out increased embryo size as an explanation for the rescue of the HPE phenotypes. Overall, these data suggest that *Boc* deletion in a *Gas1* mutant background partially rescues TV and MNP separation in E10.5 embryos.

To determine whether the phenotypes observed in *Gas1;Boc* mutants correlate with changes in HH pathway activity, we performed *in situ* hybridization for the direct HH transcriptional target *Gli1* in E10.5 wild-type, *Gas1*$^{-/-}$, *Boc*$^{-/-}$ and *Gas*$^{-/-}$*;Boc*$^{-/-}$ embryos (Fig. 3G-J). *Gas1*$^{-/-}$*;Boc*$^{-/-}$ embryos that display increased MNP separation also display increased *Gli1* expression in the MNP (Fig. 3J), consistent with the notion that *Boc* antagonizes HH pathway activity during craniofacial development. Similarly, *Gas1;Boc* mutants that do not display the rescue of the craniofacial defects exhibit decreased *Gli1* levels, indicating that the rescue is HH-dependent (Fig. S4M-O). We also examined *Gli1* expression in the forelimb bud from these same embryos (Fig. 3G'-J'). Although we did not observe significant differences in *Gli1* gene expression or GLI1 protein levels in *Gas1* or *Boc* single mutants (Fig. S6), we did detect decreased *Gli1* expression in *Gas1;Boc* double mutant embryos (see Fig. 3G′,H′,J′). Together, these data suggest that loss of *Boc* partially and selectively rescues HPE phenotypes observed in *Gas1* mutant embryos, through increased HH pathway activity specifically in craniofacial structures.

To examine the consequences of *Boc* deletion on additional targets of the HH pathway, and to begin to dissect possible tissue-specific contributions to craniofacial development, we investigated HH-dependent neural patterning in both the developing forebrain and spinal cord (Fig. 4A-L). Specifically, we used whole-mount immunofluorescence to analyze the expression of NKX2.1, a direct HH transcriptional target in the ventral telencephalon (Pabst et al., 2000) (Fig. 4E-H,M). In E10.5 *Gas1*$^{-/-}$ embryos, the expression domain of NKX2.1 is significantly reduced (Fig. 4F), whereas NKX2.1 expression in *Boc*$^{-/-}$ embryos is unchanged compared with wild-type embryos (see Fig. 4E,G). Notably, compared with *Gas1*$^{-/-}$ embryos (Fig. 4F), *Gas1*$^{-/-}$*;Boc*$^{-/-}$ embryos maintain similar levels of NKX2.1 expression (Fig. 4H). Quantitation confirms that NKX2.1 is not significantly altered in *Gas1*$^{-/-}$*;Boc*$^{-/-}$ embryos compared with *Gas1*$^{-/-}$ embryos (Fig. 4M). We also confirmed that NKX2.1 is not significantly different in *Boc*$^{-/-}$ embryos (Fig. 4M). Together, these data suggest that, despite its broad expression in the forebrain NE (Fig. 1T), *Boc* does not positively contribute to HH-dependent patterning in this tissue. These data do raise the question of whether *Boc* can regulate HH signaling in the developing telencephalon, or whether it may be playing an antagonistic role. To address these possibilities, we used chicken *in ovo* telencephalon electroporations to assess *Boc* function during HH-dependent neural patterning in the forebrain (Fig. S7). Expression of GFP (pCIG, empty vector) in the chicken telencephalon does not affect NKX2.1 expression (Fig. S7A-D). In contrast, expression of SmoM2 (a constitutively active form of SMO) (Xie et al., 1998), which drives high levels of HH pathway activity, induces ectopic NKX2.1 expression (Fig. S7E-H). Similarly, expression of *Boc* also induces ectopic NKX2.1 expression (Fig. S7I-L). These data demonstrate that *Boc* can promote HH-dependent patterning in the developing chicken forebrain and suggest that *Boc* does not play an antagonistic role in the forebrain NE.

We also analyzed HH-dependent neural patterning in the spinal cord of wild-type, *Gas1*$^{-/-}$, *Boc*$^{-/-}$ and *Gas1*$^{-/-}$*;Boc*$^{-/-}$ embryos (Fig. 4I-L,N). We examined the expression of NKX2.2 and OLIG2, two direct HH transcriptional targets that are activated in response to high and moderate levels of SHH signaling, respectively (Briscoe et al., 2000; Dessaud et al., 2008). At E10.5, *Gas1*$^{-/-}$ embryos displayed a significant reduction in the number of NKX2.2+ cells compared with wild-type embryos (Fig. 4J,N). In contrast, the number of NKX2.2+ cells was not significantly reduced in *Boc*$^{-/-}$ embryos (Fig. 4K,N). Strikingly, *Gas1*$^{-/-}$*;Boc*$^{-/-}$ embryos had a very severe phenotype – OLIG2 expression was completely absent (Fig. 4L), and we observed a near complete absence of NKX2.2 expression (Fig. 4L,N). In some sections from *Gas1;Boc* mutants we could detect a few NKX2.2+ cells (Fig. 4L, inset). Overall, these data are consistent with previous studies (Allen et al., 2011), and further demonstrate that *Boc* selectively contributes to spinal cord, but not forebrain, neural patterning.

Given that E10.5 *Gas1*$^{-/-}$*;Boc*$^{-/-}$ mutants manifest a partial rescue of the craniofacial defects observed in *Gas1* single mutants, we investigated whether this rescue is maintained over developmental time. This question is particularly relevant as a previous analysis of *Gas1*$^{-/-}$*;Boc*$^{-/-}$ embryos maintained on a mixed 129sv/C57BL/6/CD1 background demonstrated severe craniofacial defects such as clefting of the lip, palate and tongue, and disruption of the maxillary incisor (Seppala et al., 2014). To address this question, we examined craniofacial development in E18.5 wild-type and mutant embryos (Fig. 5A-D,M-P). Consistent with previous work, E18.5 *Gas1*$^{-/-}$ embryos display a range of craniofacial defects, whereas *Boc*$^{-/-}$ embryos appear phenotypically normal (Fig. 5A-C,M-O, Fig. S8A,B,H,I) (Allen et al., 2011, 2007; Martinelli and Fan, 2007; Seppala et al., 2007, 2014; Zhang et al., 2011). *Gas1*$^{-/-}$ and *Gas1*$^{-/-}$*;Boc*$^{-/-}$ embryos share defects that include microphthalmia, midface and mandible hypoplasia, and cleft palate (Martinelli and Fan, 2007). Strikingly, and similar to what was observed during earlier developmental stages, E18.5 *Gas1*$^{-/-}$*;Boc*$^{-/-}$ mutants display a less severe phenotype in specific craniofacial structures (Fig. 5D,P). Specifically, *Gas1*$^{-/-}$*;Boc*$^{-/-}$ mutants display a wider maxilla and partial separation of the nasal pits; in comparison, *Gas1*$^{-/-}$ embryos have a smaller maxilla and no separation of the nasal pits (compare black and white arrows in Fig. 5B,D). Skeletal preparations (Fig. 5E-L) confirm that *Gas1*$^{-/-}$*;Boc*$^{-/-}$ mutants exhibit separation of the nasal capsule, whereas in *Gas1*$^{-/-}$ single mutants, the nasal capsule is not separated (Fig. 5F,H). In addition to the nasal capsule, some *Gas1*$^{-/-}$*;Boc*$^{-/-}$ embryos exhibit widening of the premaxilla, although in others, it is hypoplastic (see red arrow in Fig. 5H and inset in Fig. S8J). These data suggest that the amelioration of the craniofacial defects observed at E10.5 in *Gas1;Boc* mutant embryos persists over developmental time.

In contrast to the nasal capsule and premaxilla, *Gas1*$^{-/-}$*;Boc*$^{-/-}$ embryos exhibit a shortened mandible and truncated Meckel's cartilage compared with *Gas1*$^{-/-}$ embryos (Fig. 5J,L). The mandible of *Gas1*$^{-/-}$*;Boc*$^{-/-}$ mutants also exhibits ectopic bone duplications on the posterior inferior side of the mandible (Fig. 5L). Occasionally, *Gas1*$^{-/-}$ mutants with severe HPE phenotypes display a similar phenotype (Fig. 5J inset). Bone duplications have been associated with loss of HH signaling in the mandibular neural crest-derived mesenchyme (Jeong et al., 2004; Xu et al., 2019). *Gas1*$^{-/-}$*;Boc*$^{-/-}$ mutants also display severe defects in the maxilla, palatine bone and the occipital bone (Fig. S8J). We also evaluated SHH-dependent digit specification in these embryos (Fig. S8G′-J′). Consistent with previous work (Allen et al., 2011), combined loss of *Gas1* and *Boc* results in severe digit specification defects (Fig. S8J′). These results suggest opposing and tissue-specific contributions of *Boc* to HH-dependent craniofacial development.

Development (2020) 147, dev189076. doi:10.1242/dev.189076

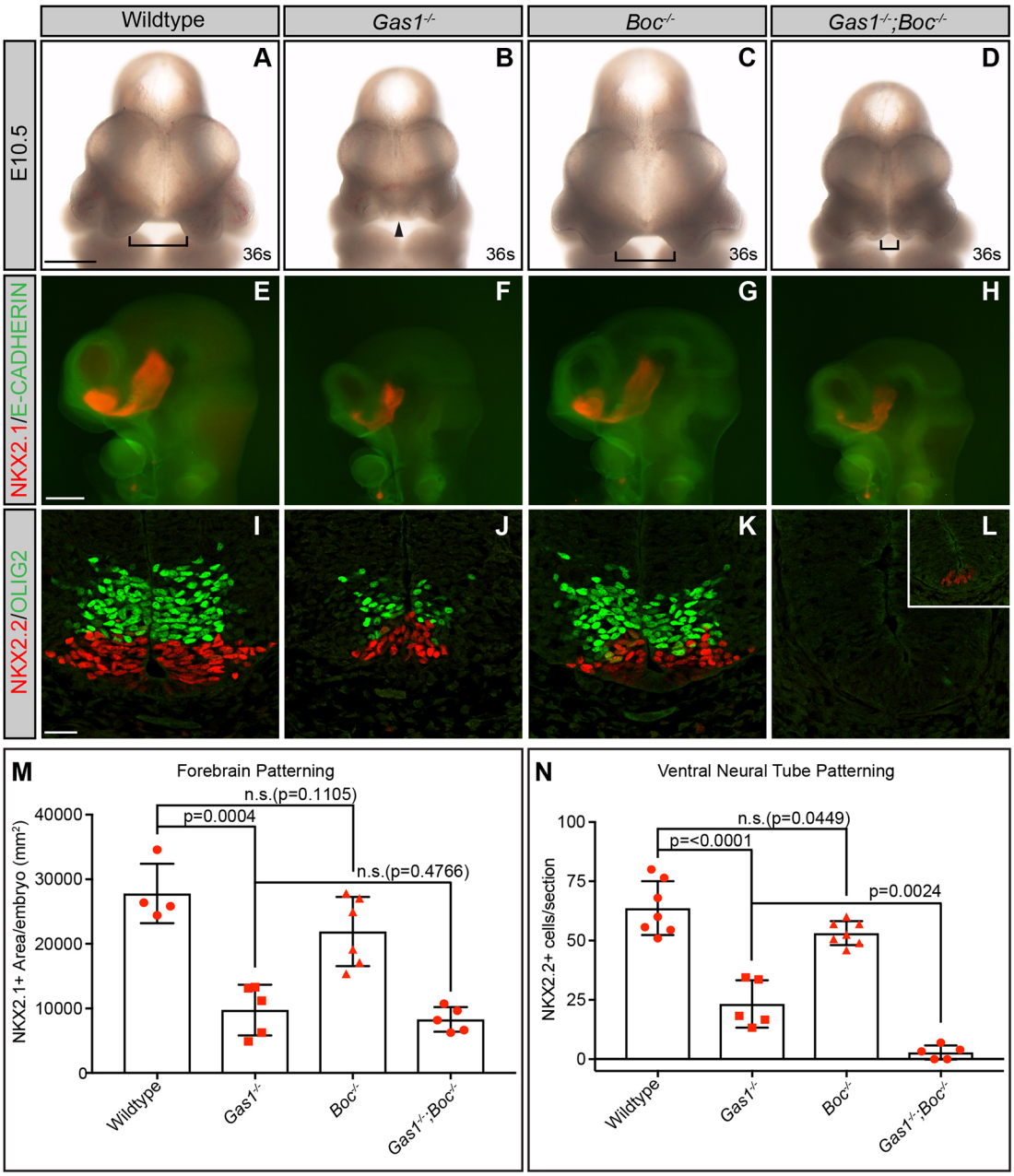

Fig. 4. Selective contribution of *Boc* to patterning of the neural tube but not the forebrain NE. (A-D) *En face* view of E10.5 wild-type (A), *Gas1*$^{-/-}$ (B), *Boc*$^{-/-}$ (C) and *Gas1*$^{-/-}$;*Boc*$^{-/-}$ (D) embryos. Somite number (s) is indicated in the lower right corner of each panel. Brackets indicate internasal distance. Arrowhead denotes fusion of the medial nasal process. (E-H) Whole-mount immunofluorescent antibody detection of E-cadherin (green) and NKX2.1 (red) in E10.5 wild-type (E), *Gas1*$^{-/-}$ (F), *Boc*$^{-/-}$ (G) and *Gas1*$^{-/-}$;*Boc*$^{-/-}$ (H) embryos. (I-L) Antibody detection of OLIG2 (green) and NKX2.2 (red) in transverse sections of E10.5 forelimb-level neural tubes from wild-type (I), *Gas1*$^{-/-}$ (J), *Boc*$^{-/-}$ (K) and *Gas1*$^{-/-}$;*Boc*$^{-/-}$ (L) embryos. (M) Quantitation of NKX2.1 expression in wild-type (n=4), *Gas1*$^{-/-}$ (n=5), *Boc*$^{-/-}$ (n=6) and *Gas1*$^{-/-}$;*Boc*$^{-/-}$ (n=5) embryos. (N) Quantitation of NKX2.2+ cells (two sections/embryo) for wild-type (n=7), *Gas1*$^{-/-}$ (n=5), *Boc*$^{-/-}$ (n=7) and *Gas1*$^{-/-}$;*Boc*$^{-/-}$ (n=5) embryos. Data are mean±s.d. P-values were determined using a two-tailed Student's t-test. The Bonferroni correction was employed to account for multiple comparisons in each dataset; (M,N) non-significant (n.s.; P>0.0166), significant (P≤0.0166). Note that NKX2.2+ cells are only present in a subset of sections from *Gas1*$^{-/-}$;*Boc*$^{-/-}$ embryos (inset in L). Scale bars: 500 µm in A,E; 25 µm in I.

To further investigate these phenotypes, we analyzed three-dimensional (3D) reconstructions from micro-computed tomography (µCT) images (Fig. 5M′-P′, Fig. S8A′-D′). Specifically, we focused on the nasal bone, in which we observed the partial rescue in *Gas1;Boc* mutants. The 3D reconstructions indicated that the nasal bone in *Gas1*$^{-/-}$;*Boc*$^{-/-}$ embryos is reduced in size and partially fused when compared with wild-type embryos (Fig. 5M′,P′). As we observed at E10.5 (Fig. 2), there is a spectrum of HPE phenotypes in *Gas1* mutants, ranging from reduced and fused nasal bone to fragments of nasal bone (Fig. 5N′, Fig. S8A′-B′). *Gas1;Boc* mutants display an intermediate nasal bone phenotype when compared with the spectrum of phenotypes in *Gas1* single mutants (Fig. 5N′,P′, Fig. S8A′-D′).

Quantitation of head width in E18.5 embryos demonstrates that *Gas1;Boc* mutants display a significantly narrower head compared with *Gas1* mutants (Fig. S9A,B), consistent with our observations at

Development (2020) 147, dev189076. doi:10.1242/dev.189076

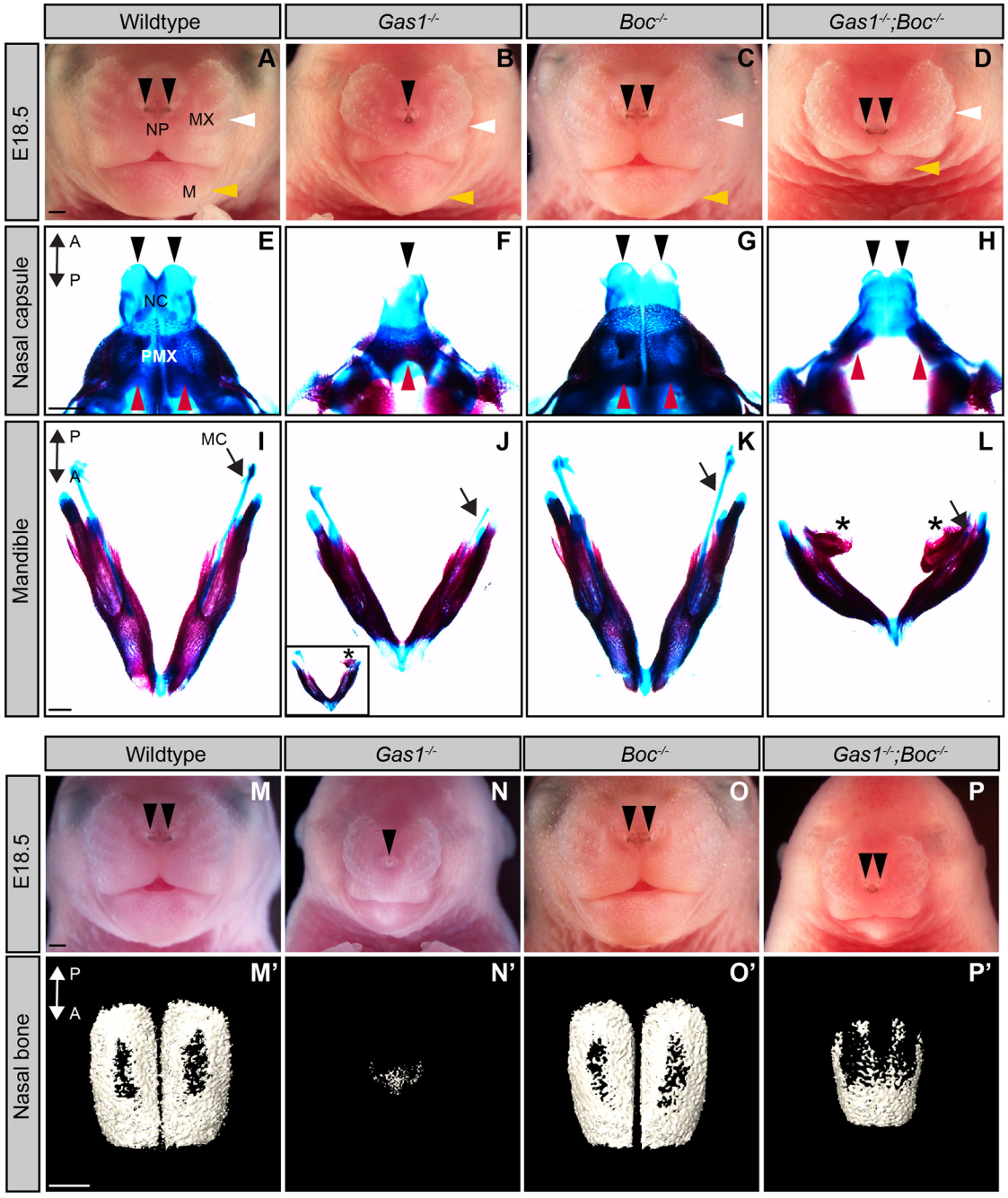

Fig. 5. Partial rescue of HPE phenotypes persists through E18.5 in *Gas1;Boc* mutant embryos. (A-D,M-P) *En face* view of E18.5 wild-type (A,M), *Gas1*$^{-/-}$ (B,N), *Boc*$^{-/-}$ (C,O) and *Gas1*$^{-/-}$;*Boc*$^{-/-}$ (D,P) embryos. Black arrowheads denote the nasal pits (NP); white arrowheads mark the maxilla (MX); yellow arrowheads identify the mandible (M). (E-L) E18.5 craniofacial structures stained with Alcian Blue and Alizarin Red to visualize cartilage and bone, respectively. Dorsal views of the nasal capsule (NC) and premaxilla (PMX) of E18.5 wild-type (E), *Gas1*$^{-/-}$ (F), *Boc*$^{-/-}$ (G) and *Gas1*$^{-/-}$;*Boc*$^{-/-}$ (H) are shown. Black arrowheads indicate the nasal capsule; red arrowheads mark the premaxilla. Dorsal views of the mandible of E18.5 wild-type (I), *Gas1*$^{-/-}$ (J), *Boc*$^{-/-}$ (K) and *Gas1*$^{-/-}$;*Boc*$^{-/-}$ (L) are shown. Asterisks identify ectopic bone duplications in the posterior part of the mandible; black arrows denote Meckel's cartilage (MC). Inset in J shows ectopic bone in a *Gas1*$^{-/-}$ mutant embryo. (M′-P′) 3D reconstructions of µCT images of isolated nasal bones from E18.5 wild-type (M′), *Gas1*$^{-/-}$ (N′), *Boc*$^{-/-}$ (O′) and *Gas1*$^{-/-}$;*Boc*$^{-/-}$ (P′) embryos. A↔P specifies the anterior to posterior axis. Scale bars: 500 µm.

E10.5 that *Gas1;Boc* mutant embryos trend smaller overall than *Gas1* single mutants (Fig. S5F). Accounting for this size difference, *Gas1;Boc* mutant embryos exhibit a significant increase in interocular distance when compared with *Gas1* mutant embryos (Fig. S9A,C). Examination of nostril frequency at E18.5 revealed that 100% (8/8 embryos) of *Gas1*$^{-/-}$;*Boc*$^{-/-}$ embryos display two partially fused nostrils; in contrast only 58% (7/12 embryos) of *Gas1*$^{-/-}$ embryos exhibit two partially fused nostrils, whereas 42% (5/12 embryos) display a single nostril (Fig. S9E). Finally, *Gas1;Boc* mutants exhibit a significantly wider medial lip notch distance at E18.5 than *Gas1* mutants (Fig. S9F). Taken together, these data demonstrate that *Boc* deletion in a *Gas1* mutant background significantly ameliorates several craniofacial defects at later developmental stages, consistent with the phenotypes observed at E10.5.

Development (2020) 147, dev189076. doi:10.1242/dev.189076

To investigate the mechanisms that could explain the partial rescue observed in *Gas1*$^{-/-}$;*Boc*$^{-/-}$ embryos, we analyzed tissue-specific proliferation in the forebrain of E10.5 wild-type and mutant embryos. Specifically, we performed immunofluorescence for phospho-histone H3 (PH3), and co-stained with E-cadherin (E-CAD; also known as Cdh1) and PDGFRα to discriminate between the surface ectoderm, forebrain NE and craniofacial mesenchyme (Fig. 6A-E). Coronal sections of E10.5 *Gas1*$^{-/-}$ mutant embryos display normal numbers of PH3+ cells across the surface ectoderm and forebrain NE (Fig. 6B,F,G). In the craniofacial mesenchyme *Gas1* mutant embryos display a subtle increase in PH3+ cells that fails to reach statistical significance (Fig. 6H). *Cdon*$^{-/-}$ embryos do not exhibit any significant changes in proliferation in any of the craniofacial tissues (Fig. 6F-H). Similarly, *Boc*$^{-/-}$ embryos do not display any apparent changes in proliferation in the surface ectoderm or in the NE (Fig. 6F,G). However, *Boc*$^{-/-}$ embryos do display a significant increase in mesenchymal proliferation compared with wild-type embryos (Fig. 6D,H). These results suggest that *Boc* negatively regulates proliferation specifically in craniofacial mesenchyme.

We also investigated tissue-specific proliferation in *Gas1*$^{-/-}$;*Boc*$^{-/-}$ mutant embryos. Notably, the levels of proliferation in the surface ectoderm and the forebrain NE were not significantly different when compared with wild-type or *Gas1*$^{-/-}$ embryos (Fig. 6F-G). In contrast, proliferation was significantly increased in the craniofacial mesenchyme of *Gas1;Boc* mutants when compared with wild-type embryos, although not when compared with *Gas1* mutants. (Fig. 6H). Surprisingly, this effect on proliferation appears to be quite selective, as there were no significant changes in proliferation in either the neural tube or the forelimb mesenchyme (Fig. S10). Overall, these data suggest that *Boc* functions in a non-redundant manner to restrict proliferation in the craniofacial mesenchyme.

DISCUSSION

Here, we investigated the individual and combined contributions of the HH co-receptors *Gas1*, *Cdon* and *Boc* during HH-dependent craniofacial development. We found that *Boc* displays a significantly broader expression pattern than *Gas1* and *Cdon* in multiple craniofacial structures. Surprisingly, and distinct from *Gas1* and *Cdon*, loss of *Boc* results in facial widening and increased HH pathway activity in the nasal processes (Brugmann et al., 2010; Hu and Helms, 1999). Further, analysis of *Gas1;Boc* double mutants revealed an amelioration of the craniofacial phenotype observed in *Gas1* single mutants, corresponding with increased HH pathway activity, and consistent with the notion that loss of *Boc* can counterintuitively drive increased HH signaling. Notably, this improvement is restricted to a subset of craniofacial structures, but persists throughout embryonic development. Mechanistic analyses suggest that *Boc* selectively restricts proliferation in neural crest-derived mesenchyme and limits HH pathway activity in the nasal processes. Taken together, these data demonstrate that *Boc* regulates HH signaling in a tissue-specific manner, and suggests that, in certain tissues, BOC works in opposition to other HH co-receptors to restrain HH pathway function.

Genetic background-dependent phenotypic differences in HH co-receptor mutants

Understanding the molecular mechanisms that underlie HPE is confounded by the significant phenotypic variability observed in

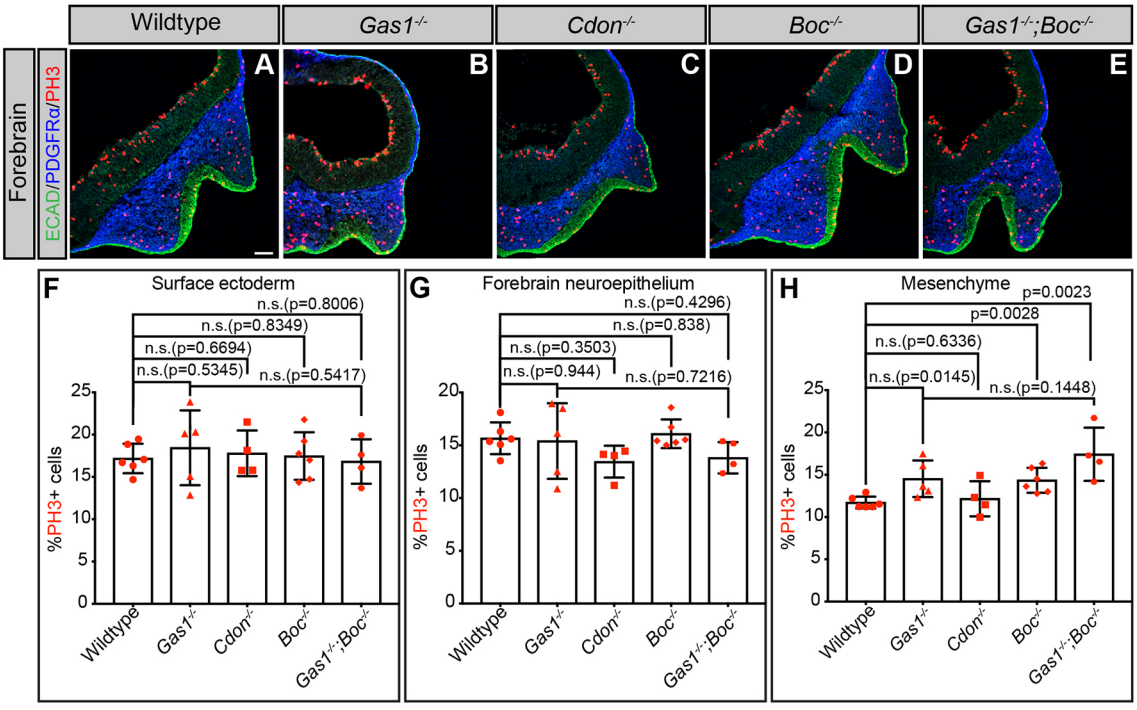

Fig. 6. *Boc* selectively inhibits mesenchymal proliferation during craniofacial development. (A-E) Immunofluorescent analysis of proliferation in E10.5 forebrain coronal sections from wild-type (A), *Gas1*$^{-/-}$ (B), *Cdon*$^{-/-}$ (C), *Boc*$^{-/-}$ (D) and *Gas1*$^{-/-}$;*Boc*$^{-/-}$ (E) embryos. Antibody detection of E-cadherin (ECAD, green), PDGFRα (blue) and phospho-histone H3 (PH3, red). (F-H) Quantitation of PH3+ cells (two sections/embryo) normalized to the total number of DAPI+ cells in the quantified areas of surface ectoderm (F), forebrain NE (G) and craniofacial mesenchyme (H) of E10.5 wild-type (n=6), *Gas1*$^{-/-}$ (n=5), *Boc*$^{-/-}$ (n=6) and *Gas1*$^{-/-}$;*Boc*$^{-/-}$ (n=4). Data are mean±s.d. P-values were determined using a two-tailed Student's t-test. The Bonferroni correction was employed to account for multiple comparisons in each dataset; (F-H) non-significant (n.s.; P>0.0125), significant (P≤0.0125). Note that *Boc*$^{-/-}$ embryos display increased proliferation in the craniofacial mesenchyme (H). Scale bar: 50 µm.

Development (2020) 147, dev189076. doi:10.1242/dev.189076

this disease, and the complex genetics that contribute to proper craniofacial development. Our data indicate that, even when maintained on a congenic C57BL/6J background, *Gas1* and *Cdon* mutants display a range of HPE phenotypes. These phenotypes vary from microforms of HPE to semilobar HPE, and their severity correlates with HH pathway activity as assessed by *Gli1* expression. The variability in the HPE phenotypes of our mutants could be explained due to multiple genetic and non-genetic risk factors (Hong and Krauss, 2018). In particular, the variable severity across the phenotypes in our mutants could arise from stochastic changes in the establishment or response to the SHH morphogen gradient in the NE, neural crest-derived mesenchyme and/or surface ectoderm. In early craniofacial structures *Shh* is expressed sequentially, initiating in the prechordal plate, followed by the diencephalon and telencephalon, subsequently in the surface ectoderm of the frontonasal prominence, and finally in the pharyngeal endoderm of the first branchial arch (Aoto et al., 2009; Cordero et al., 2004; Marcucio et al., 2005; Rubenstein and Beachy, 1998; Xavier et al., 2016a). This complex developmental expression sequence of *Shh*, which is required to properly pattern the craniofacial structures (Krauss, 2007), combined with the differential expression of multiple HH receptors could generate an inherent variability that affects the severity of the HPE phenotypes.

The lack of craniofacial defects in *Boc* mutants maintained on different genetic mixed backgrounds (Okada et al., 2006; Seppala et al., 2014; Zhang et al., 2011) suggests a minor, redundant role for *Boc* in HH-dependent craniofacial development. This notion of *Boc* as a silent HPE modifier gene is supported by studies in which *Boc* deletion in a *Gas1* or *Cdon* null background enhances HPE severity and decreases the levels of HH pathway targets (Seppala et al., 2014; Zhang et al., 2011). However, our data indicate that *Boc* mutants on a C57BL/6J background exhibit internasal distance widening in E10.5 embryos and increased *Gli1* expression specifically in the nasal processes. These data suggest an antagonistic role for *Boc* in HH signaling during craniofacial development. Previous studies described *Boc* as a potential HH pathway antagonist in the zebrafish lower jaw (Bergeron et al., 2011). However, this study is limited to a brief phenotypic description of the thickening and expansion of the cartilage elements in the lower jaw of *Boc* (*umleitung*) zebrafish mutants; it does not examine the effects of *Boc* deletion on HH pathway activity in this tissue. Although we do not observe any mandible phenotypes in $Boc^{-/-}$ embryos, species-specific differences in craniofacial development between mouse and fish likely limit our ability to draw a direct connection. Alternatively, our analysis of *Boc* in the developing mandible may not be comprehensive enough to reveal this function. Regardless, our data reveal a novel, antagonistic role for *Boc* during aspects of craniofacial development, and raises the question of whether BOC may work in concert with other known redundant HH pathway antagonists, including PTCH1, PTCH2 and HHIP1, to maintain the balance between HH pathway activation and inhibition (Holtz et al., 2013) in the craniofacial structures. In addition, our data suggest that HH co-receptors can function to alternately promote or antagonize HH signaling depending on the context. In support of this notion, *Gas1* can antagonize HH signaling in presomitic mesoderm explants (Lee et al., 2001), and restricts HH signaling during tooth development in mice (Cobourne et al., 2004; Ohazama et al., 2009). Similarly, *Cdon* negatively regulates HH pathway function in the optic vesicle of zebrafish and chick embryos (Cardozo et al., 2014).

Boc deletion partially rescues the HPE phenotypes of *Gas1* single mutants. Specifically, *Gas1;Boc* double mutants display increased MNP separation at E10.5, and increased interocular distance, partially restored nostril frequency, and broader medial lip notch distance at E18.5. Importantly, these phenotypes correlate with increased *Gli1* levels in the MNP and increased proliferation in the neural crest mesenchyme. Although the combination of these tissue-specific effects could mediate the rescue of the craniofacial defects in *Gas1;Boc* mutants, the incomplete penetrance of the rescue indicates that the variable HPE phenotypes observed in *Gas1* single mutants also impacts the degree of rescue. Overall, this suggests a more complex mechanism, in which genetic, epigenetic and environmental cues all contribute to proper craniofacial development. Along these lines, our data partially contrast with previous work (Seppala et al., 2014), in which *Gas1;Boc* mutants on a 129Sv-C57BL/6/CD1 genetic background display more severe phenotypes than those observed in *Gas1* mutants (Seppala et al., 2014). Although *Gas1;Boc* mutants on a C57BL/6J background display severe defects in the majority of the bones of the skull and cleft palate as previously reported (Seppala et al., 2014), we never observe clefting of the lip in these mutants. Given that the lip is formed by the fusion of the MXP and the nasal processes (Jiang et al., 2006), this result is consistent with the partial rescue mediated by *Boc* deletion in the nasal bone and nasal capsule.

Tissue-specific functions of Boc in HH signal transduction

Analysis of HH transcriptional targets revealed that *Boc* deletion results in differential changes in HH-dependent gene expression in a tissue-specific fashion (Fig. 7A). Specifically, our data suggest that BOC promotes the expression of the direct HH transcriptional target, NKX2.2, in the spinal cord NE, but does not contribute to expression of NKX2.1 in the telencephalon NE. These data suggest that BOC differentially regulates HH-dependent neural patterning at distinct axial levels. In the surface ectoderm, BOC does not impact proliferation; further experiments will be required to determine whether BOC contributes to patterning of this tissue (Fig. 7A). Further, BOC promotes *Gli1* expression in the limb bud mesenchyme but antagonizes *Gli1* expression in the forebrain mesenchyme. Notably, *Boc* appears to selectively impact HH-dependent patterning, but not proliferation in the developing limb bud; conversely, *Boc* selectively inhibits proliferation in the neural crest-derived mesenchyme of the craniofacial structures (Fig. 7A). This is consistent with previous work by (Xavier et al., 2016b) suggesting that *Boc* contributes to mesenchymal proliferation in the palatal shelf. Taken together, these data argue that BOC regulates patterning and proliferation in a tissue-specific manner and raises the possibility that BOC performs multiple, and in some cases opposing, roles in HH signal transduction.

Boc as a multi-functional regulator of HH signaling

Based on our data, and the work of others, we propose a model whereby BOC acts as a multi-functional receptor to contribute to vertebrate embryogenesis (Fig. 7B). Specifically, we propose that BOC can act to: (1) promote HH signaling through interactions with HH ligands and the canonical receptor PTCH1; (2) antagonize HH signaling, either through ligand sequestration, or perhaps through the formation of an inhibitory complex with PTCH1; (3) contribute to HH-dependent signaling via its unique cytoplasmic domain; (4) function independently of the HH pathway.

BOC physically interacts with PTCH1 in an SHH-independent manner (Izzi et al., 2011). In craniofacial structures PTCH1 and BOC are both expressed in the MNP (Seppala et al., 2014). The differential interaction of these proteins could allow the formation of a receptor complex that alternately activates or inhibits HH pathway

Development (2020) 147, dev189076. doi:10.1242/dev.189076

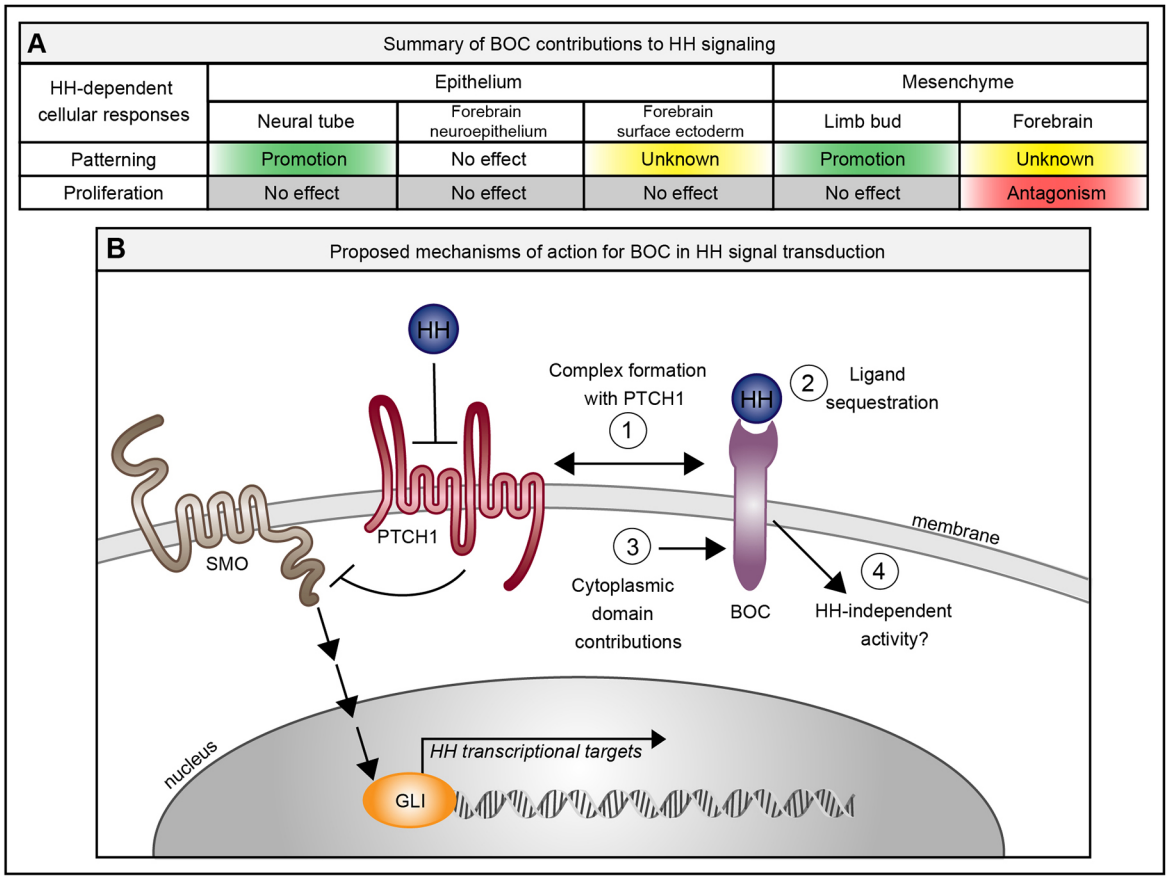

Fig. 7. BOC is a multi-functional regulator of HH signaling. (A) Summary of BOC contributions to HH signaling. Green indicates promotion of HH signaling; red denotes HH pathway antagonism; gray suggests no effect; yellow is unknown. (B) Proposed mechanisms of action for BOC in HH signal transduction. (1) Complex formation with PTCH1: the interaction of PTCH1 and BOC that allows the formation of a receptor complex that alternately activates or inhibits HH pathway activity. (2) Ligand sequestration: BOC binds HH ligands through its extracellular domain and could antagonize HH signaling by sequestering SHH in areas of low SHH concentration. (3) Cytoplasmic domain contributions: the unique cytoplasmic domain of BOC could regulate additional downstream signaling cascades that enable its tissue-specific functions. (4) HH-independent activity: BOC could mediate yet-to-be-identified HH-independent functions that either augment or counter the HH response.

activity. Alternatively, BOC binding to HH ligands via its extracellular domain (Beachy et al., 2010; McLellan et al., 2008; Yao et al., 2006) raises the possibility that BOC can sequester SHH ligand in areas of low SHH concentration, and subsequently antagonize HH signaling. Consistent with this notion, *Boc* expression in HH-responsive tissues generally extends closer to the source of the SHH ligand than either *Gas*1 or *Cdon*. In particular, at E10.5 *Boc* is expressed in the surface ectoderm of the MNP, in which *Shh* is also expressed (Xavier et al., 2016a). Loss of *Boc* in the MNP could allow for the expansion of SHH protein distribution, resulting in increased pathway function, and subsequently in widening of the midface. This putative increased range of SHH could similarly explain the partial rescue of craniofacial defects in *Gas1;Boc* mutants compared with *Gas1* single mutants.

BOC displays a unique cytoplasmic domain that does not resemble any other protein or motif (Kang et al., 2002). Recent work suggests that the BOC cytoplasmic domain binds to the non-receptor tyrosine kinase ABL (Vuong et al., 2017) and to the adaptor protein ELMO1 (Makihara et al., 2018). Thus, this domain could be crucial to mediate tissue-specific HH-dependent signals, or to perform HH-independent functions through the activation of downstream signaling cascades. Future work will be required to determine potential contributions of these mechanisms to BOC tissue-specific functions during craniofacial development. Overall, this work identifies multiple and distinct roles for BOC in HH-dependent craniofacial development.

MATERIALS AND METHODS

Reagents

General reagents (Table S1), primary and secondary antibodies for immunofluorescence (Table S2), western blot analysis antibodies (Table S3) and qRT-PCR primer sequences (Table S4) are provided in Supplementary information.

Animal models

Gas1^{lacZ} (Martinelli and Fan, 2007), *Cdon*$^{lacZ-2}$ (Cole and Krauss, 2003) and *Boc*^{AP} (Zhang et al., 2011) mice have been all described previously. *Gas1*, *Cdon* and *Boc* mutants were backcrossed for at least ten generations to create lines on a congenic C57BL/6J background. *Cdon*$^{lacZ-1}$ mice (Cole and Krauss, 2003) were maintained on a mixed 129/Sv/C57BL/6J background for expression analysis. For embryonic dissections, noon of the day on which a vaginal plug was detected was considered as E0.5. For precise staging, somites were counted during the dissection. Embryos with 34-38 somites were considered E10.5 embryos. Fertilized eggs were obtained from the Poultry Teaching and Research Center at Michigan State University, USA. To obtain Hamburger-Hamilton stage 11 chicken embryos, the fertilized eggs were incubated for 39-40 h at 37°C in a GQF 1550 hatcher incubator with

Development (2020) 147, dev189076. doi:10.1242/dev.189076

normal humidity settings (45%-55%). All animal procedures were reviewed and approved by the Institutional Animal Care and Use Committee (IACUC) at the University of Michigan, USA.

X-gal staining

Embryos were dissected in 1× PBS (pH 7.4) and fixed (1% formaldehyde, 0.2% glutaraldehyde, 2 mM $MgCl_2$, 5 mM EGTA, 0.02% NP-40) on ice for 10-60 min depending on the embryonic stage. Subsequently, the embryos were washed 3×5 min with 1× PBS (pH 7.4)+0.02% NP-40 for permeabilization. β-Galactosidase activity was detected with X-gal staining solution [5 mM $K_3Fe(CN)_6$, 5 mM $K_4Fe(CN)_6$, 2 mM $MgCl_2$, 0.01% Na deoxycholate, 0.02% NP-40, 1 mg/ml X-gal]. The signal was developed from 25 min to 24 h at 37° C depending on the *lacZ* allele. After staining, the embryos were washed 3×5 min with 1× PBS (pH 7.4) at 4°C, and post-fixed in 4% paraformaldehyde for 20 min at room temperature, followed by 3×5 min washes in 1× PBS (pH 7.4). Finally, embryos were stored and photographed in 1× PBS (pH 7.4)+50% glycerol. X-gal staining of sections (20 µm) was performed as described above for whole-mount embryos. After staining, sections were washed 3×5 min with 1× PBS (pH 7.4), counterstained with Nuclear Fast Red for 5 min and dehydrated in an ethanol series (70% ethanol, 95% ethanol, 100% ethanol and 100% xylene) followed by application of coverslips with Permount Mounting Medium (Thermo Fisher Scientific).

AP staining

Embryos were dissected in 1× PBS (pH 7.4) and fixed (1% formaldehyde, 0.2% glutaraldehyde, 2 mM $MgCl_2$, 5 mM EGTA, 0.02% NP-40) on ice for 10-60 min depending on the embryonic stage. Subsequently, the embryos were washed 3×5 min with 1× PBS (pH 7.4). To deactivate endogenous AP, embryos were incubated in 1× PBS (pH 7.4) at 70°C for 30 min. Then the embryos were rinsed with 1× PBS (pH 7.4) and washed for 10 min in AP buffer [100 mM NaCl, 100 mM Tris-HCl (pH 9.5), 50 mM $MgCl_2$, 1% Tween-20] at room temperature. Embryos were stained with BM Purple for 2-3 h at 37°C depending on the embryonic stage. After staining, the embryos were washed 3×5 min with 1× PBS (pH 7.4) at 4°C, and post-fixed in 4% paraformaldehyde for 20 min at room temperature, followed by 3×5 min washes with 1× PBS (pH 7.4). Finally, embryos were stored and photographed in 1× PBS (pH 7.4)+50% glycerol. AP staining of sections (20 µm) was performed as described above for whole-mount embryos. After staining, sections were washed 3×5 min with 1× PBS (pH 7.4), counterstained with Nuclear Fast Red for 5 min and dehydrated in an ethanol series (70% ethanol, 95% ethanol, 100% ethanol and 100% xylene for 5 min each) followed by application of coverslips with Permount Mounting Medium.

Whole-mount digoxigenin *in situ* hybridization

Whole-mount digoxigenin *in situ* hybridization was performed as previously described (Allen et al., 2011; Wilkinson, 1992). In brief, embryos were dissected in 1× PBS (pH 7.4) and fixed in 4% paraformaldehyde overnight on a rocking platform. After fixation, embryos were dehydrated in a methanol/PBST [1× PBS (pH 7.4)+0.1% Tween] series (25% methanol, 50% methanol, 75% methanol) and stored in 100% methanol at −20°C for up to 6 months, until the experiment was performed. Embryos were digested with 10 µg/ml proteinase K at room temperature for 2 min. Hybridization was performed with the indicated digoxigenin probe with a concentration of 1 ng/µl for 16-19 h at 70°C. The embryos were incubated in AP-conjugated anti-DIG antibody at a dilution of 1:4000. AP-anti-DIG was detected with BM Purple, and signal was developed for 3.5 h at room temperature. Embryos were cleared in 50% glycerol in 1× PBST and were photographed using a Nikon SMZ1500 microscope.

Immunofluorescence

Section immunofluorescence was performed as in Allen et al. (2011). Embryos were dissected in 1× PBS (pH 7.4) and fixed for 1 h in 4% paraformaldehyde on ice, followed by 3×5 min washes with 1× PBS (pH 7.4) and cryoprotected for 24-48 h in 1× PBS+30% sucrose. Embryos were embedded in OCT compound and sectioned on a Leica CM1950 cryostat (12 µm thick forebrain and forelimb neural tube sections). Sections were blocked in blocking buffer [3% bovine serum albumin, 1% heat-inactivated sheep serum, 0.1% Triton X-100 in 1× PBS (pH 7.4)] for 1 h. Primary antibodies were diluted in blocking buffer incubated overnight at 4°C in a humidified chamber. A list of all the primary and secondary antibodies used in this study is provided in Table S2. Secondary antibodies were diluted in blocking solution and incubated for 1 h at room temperature, followed by 3×5 min washes with 1× PBS (pH 7.4). All Alexa Fluor Dyes secondary antibodies were used at a 1:500 dilution. Nuclei were labeled with DAPI for 10 min at room temperature and slides were mounted with coverslips using Immu-mount aqueous mounting medium (Thermo Fisher Scientific). Sections were visualized on a Leica SP5X upright confocal (2 photon).

Whole-mount immunofluorescence

Embryos were dissected in 1× PBS (pH 7.4), fixed with 4% paraformaldehyde for 2 h at 4°C, and washed 2×10 min washes with PBTX (1× PBS+0.1% Triton X-100). Subsequently, embryos were blocked for 1 h in PBTX+10% goat serum. Primary antibodies were diluted in PBTX+10% goat serum and incubated overnight at 4°C on a rocking platform. A list of all the primary and secondary antibodies used in this study is provided in Table S2. The next day the embryos were rinsed 2×5 min with PBTX, followed by 3×1 h washes with PBTX on a rocking platform at 4°C. After the washes, embryos were incubated overnight with secondary antibodies diluted in PBTX+ 10% serum. All Alexa Fluor Dyes secondary antibodies were used at a 1:500 dilution. Next, embryos were washed as described for the primary antibody above, and cleared with *Clear*^{T2} [25% formamide/10% polyethylene glycol (PEG) for 1 h; 50% formamide/20% PEG for 72 h] (Kuwajima et al., 2013). Finally, embryos were visualized on a Nikon SMZ1500 microscope. With the *Clear*^{T2} reagent we did not observed any tissue expansion. (Protocol courtesy of Jean-Denis Bénazet, University of California, San Francisco, USA.)

µCT

E18.5 embryos were skinned and eviscerated. Subsequently, embryos were fixed overnight in 100% ethanol, and maintained in 70% ethanol until ready to scan. The scans were performed using embryos covered with a 1× PBS (pH 7.4)-soaked kim wipe and scanned over the entire length of the skull using the µCT100 system (Scanco Medical). Scan settings were as follows: 12 µm voxel size, 55 kVp, 109 µA, 0.5 mm AL filter, and 500 ms integration time. µCT scans were analyzed using Amira software (Thermo Fisher Scientific). The µCT scans were uploaded as DICOM files into the software and the 3D reconstructions were generated using the isosurface feature. The individual bones were manually segmented using the extract surface and buffer tools of Amira (Ho et al., 2015). Finally, the individual bones were color coded.

Skeletal preparation

Skeletons were prepared as previously described (Allen et al., 2011). E18.5 embryos were skinned and eviscerated. Subsequently, embryos were fixed in 100% ethanol, followed by 100% acetone for 24 h at room temperature. Cartilage and bone were stained with Alcian Blue/Alizarin Red staining solution (5% Alcian Blue, 5% Alizarin Red, 5% glacial acetic acid and 70% ethanol) for 4 days at room temperature. The remaining tissue was digested with several washes of 1% potassium hydroxide. The skeletons were cleared by 24 h washes of a gradient of glycerol (20%, 50% and 80%) in 1% potassium hydroxide, and photographed in 80% glycerol.

In ovo chicken electroporations

Chicken electroporations were performed as previously described (Allen et al., 2011; Tenzen et al., 2006). The indicated construct [pCIG plasmid −1 µg/µl in 1× PBS (pH 7.4), with 50 ng/µl fast green] was injected into the forebrain cavity of Hamburger-Hamilton stage 11 chicken embryos. L-shaped electrodes were made with platinum wire, 8 mm long (3 mm was bent to form the L shape) and spaced 1 mm apart. Electrodes (L-shaped part) were placed in front of the forebrain of the embryo (pulsed five times at 25 V for 50 ms with a BTX electroporator). The electroporated embryos were screened for GFP expression after 48 h at Hamburger-Hamilton stage 21-22 and processed for immunofluorescence.

Development (2020) 147, dev189076. doi:10.1242/dev.189076

RNA isolation and qRT-PCR

RNA was isolated from micro-dissected nasal processes (without the forebrain NE) and forelimb buds of E11.5 wild-type and mutant embryos. RNA was extracted using a Quick-RNA micro prep (Zymo Research). cDNA was generated from 500 ng and 1 µg of total RNA from the nasal process and forelimb bud mesenchyme, respectively, with a High Capacity cDNA reverse transcription kit (Applied Biosystems). qRT-PCR was performed with PowerUP SYBR Green Master Mix (Applied Biosystems) in a Step One Plus Real-Time PCR System (Applied Biosystems). qRT-PCR primers used in this paper are listed in Table S4. Gene expression was normalized to *Gapdh,* and relative expression analyses were performed using the $2(^{-ddCT})$ method. For qRT-PCR analysis at least three biological replicates were analyzed in triplicate.

Western blot analysis

E11.5 embryos were dissected in 1× PBS (pH 7.4). Nasal processes and forelimb buds were micro-dissected and incubated for 15 min and lysed in radioimmunoprecipitation assay buffer [50 mM Tris-HCl (pH 7.2), 150 mM NaCl, 0.1% Triton X-100, 1% sodium deoxycholate, 5 mM EDTA], containing a protease inhibitor cocktail (Roche). Samples were sonicated using a sonic dismembrator (model 500, Thermo Fisher Scientific) with 10 pulses of 1 s at 10% amplitude. Extracts were cleared by centrifugation at 15,000 rpm (21,130 ***g***) for 20 min at 4°C. Total protein concentration was determined using the Pierce BCA protein assay kit (Thermo Fisher Scientific), utilizing 10 µg of each sample. Lysates were mixed with 6× Laemmli buffer and boiled for 10 min at 95°C. Proteins were separated using SDS-PAGE in 5% gels and transferred onto Immuno-Blot PVDF membranes (Bio-Rad). Membranes were blocked for 1 h at room temperature in western blocking buffer [30 g/l bovine serum albumin with 0.2% NaN_3 in TBST (Tris-buffered saline, 0.5% Tween-20)]. Blots were probed with the indicated primary antibodies (Table S3) diluted in western blocking buffer and incubated overnight. After incubation in primary antibody, the membranes were rinsed 3× in TBST, followed by 3×10 min washes in TBST. Peroxidase-conjugated secondary antibodies (Table S3) were diluted in western blocking buffer and incubated for 1 h at room temperature and washed as the primary above. Membranes were incubated with Amersham ECL Prime Western Blotting Detecting Reagent (GE Healthcare) for 5 min, and exposed to HyBlot CL autoradiography film (Denville) and developed using a Konica Minolta SRX-101A medical film processor. Relative expression values were obtained by normalizing the mean gray value of each band in the blot, subtracting the background and normalizing to the mean gray value of vinculin. For relative expression analysis at least three biological replicates were analyzed.

Quantitation and statistical analysis

All the data are represented as mean±s.d. All statistical analyses were performed using GraphPad statistic calculator or GraphPad Prism (www.graphpad.com). Statistical significance was determined using two-tailed Student's *t*-test or the Fisher's exact test. Bonferroni correction was employed to account for multiple comparisons in each dataset. In brief, to account for multiple comparisons using the Bonferroni correction, the original α-value (0.05) is divided by the number of comparisons in each dataset, generating a new adjusted α-value that will determine the significance of the results. For all the experimental analyses a minimum of three embryos of each genotype were examined, each *n* represents an embryo. All the statistical details (statistical test used, adjusted *P*-value, statistical significance and exact value of each *n*) for each experiment are specified in the figure legends.

Telencephalic division and medial nasal process classification

Frontal pictures of E10.5 mouse embryos were photographed using a Nikon SMZ1500 microscope. Blind classification of the telencephalic division and media nasal process separation was performed by a blinded evaluator according the categories showed in Fig. S2A-F.

Internasal distance and CRL quantitation

Pictures of the nasal processes and whole E10.5 embryos were taken in 1× PBS (pH 7.4) using a Nikon SMZ1500 microscope. Internasal distance was defined as the distance between the edges of the medial nasal process. CRL was defined as the top of the crown of the midbrain, bisecting the forelimb bud to the curvature at the bottom c-shaped part of the embryo. Blind quantitation of the internasal distance and CRL was performed manually by a single evaluator using the scale bar tool of the NIS-Elements software (Nikon) annotations and measurements feature.

Immunofluorescence quantitation

To quantify immunofluorescence images, we examined a minimum of three embryos per genotype and two sections from each embryo. For NKX2.1 quantitation, side view pictures of whole-mount immunofluorescent wild-type and mutant embryos were taken in *Clear*^{T2} with a Nikon SMZ1500 microscope. The NKX2.1 area of expression was quantified using the area measure plugin of ImageJ (Schneider et al., 2012). Each image was thresholded automatically by ImageJ before the area of expression was quantified. For NKX2.2 quantitation, pictures of transverse sections of wild-type and mutant neural tubes stained with antibodies directed against NKX2.2 were merged with their respective DAPI images. NKX2.2-positive cells were quantified with the point tool of ImageJ (Schneider et al., 2012).

PH3 quantitation

All PH3 quantitation was performed with the point tool and analyze particle feature of ImageJ (Schneider et al., 2012). In the forebrain, the PH3-positive cells were quantified in different tissue compartments. The PH3 images were merged with markers specific to each tissue: E-cadherin (surface ectoderm) and PDGFRα (mesenchyme). The NE was identified morphologically. The dorsal telencephalic midline was excluded from this analysis. After identifying each tissue compartment with these markers and based on their morphology, we manually isolated the mesenchyme of the lateral and medial nasal process, the surface ectoderm of the olfactory epithelium and the forebrain NE with the clear outside tool of ImageJ. Each image was manually thresholded and the analyze particle feature was used to automatically quantify the PH3+ cells. DAPI+ cells were also quantified as described above to normalize the number of PH3+ cells. For the neural tube quantitation, the PH3 cells were quantified along the entire neural tube with the point tool. Finally, in the forelimb bud, the PH3+ cells were quantified using the point tool, specifically in a selected area of equal size in wild-type and mutant embryos.

µCT nasal bone width quantitation

To measure the nasal bone width of E18.5 wild-type and mutant embryos, µCT scans were imported as DICOM files into MicroView (Parallax Innovations). Three-dimensional reconstructions were generated using the Isosurface tool. All the 3D reconstructions were equally thresholded. To measure distance width, we used the built-in measure function of Parallax MicroView and measured the widest point of each nasal bone.

Quantitation of anatomical landmarks and nostril frequency

Frontal pictures of E18.5 mouse embryos were photographed in 1× PBS (pH 7.4) using a Nikon SMZ1500 microscope. Head width was defined as the widest length of the head above the eyes (Fig. S9A). Interocular distance was defined as the distance between the eyes (Fig. S9A). Snout width was denoted as the distance between the second line of most ventral vibrissae from left to right (Fig. S9A). The interocular distance and snout width was normalized to the head width. Quantitation was performed manually by a single evaluator using the scale bar tool of the NIS-Elements software (Nikon) annotations and measurements feature or using the line tool in Adobe Illustrator. The frequency of the nostrils was quantified according to the presence of partially fused nostrils with nasal pigment or a single nostril without pigment (Fig. S9E, left panel).

Acknowledgements

We thank all current and past members of the Allen lab for valuable feedback and suggestions throughout the course of this study. In particular, we thank Nicole Franks and Savannah Struble for significant technical assistance. We also thank Michelle Lynch (University of Michigan, USA) for assistance with scanning µCT samples, Thach-Vu Ho (University of Southern California, USA) for assistance with generating the µCT 3D reconstructions, Jingwen Yang (University of Michigan, USA) for assistance with nasal processes microdissection and the University of Michigan

Consulting for Statistics, Computing and Analytics Research Center for assistance with statistical analyses. We also gratefully acknowledge the Department of Cell and Developmental Biology, including the Engel, Spence, and O'Shea laboratories at the University of Michigan for providing access to research equipment. The NKX2.2 antibody was obtained from the Developmental Studies Hybridoma Bank, created by the Eunice Kennedy Shriver National Institute of Child Health and Human Development of the National Institutes of Health and maintained at The University of Iowa, Department of Biology, Iowa City, IA 52242, USA. Finally, we acknowledge the Biomedical Research Core Facilities Microscopy Core for providing access to confocal microscopy equipment, which is supported by the Rogel Cancer Center.

Competing interests
The authors declare no competing or financial interests.

Author contributions
Conceptualization: M.L.E.-A., B.L.A.; Methodology: M.L.E.-A., B.L.A.; Validation: M.L.E.-A., B.L.A.; Formal analysis: M.L.E.-A., B.L.A.; Investigation: M.L.E.-A., B.L.A.; Resources: B.L.A.; Data curation: M.L.E.-A., B.L.A.; Writing - original draft: M.L.E.-A., B.L.A.; Writing - review & editing: M.L.E.-A., B.L.A.; Visualization: M.L.E.-A., B.L.A.; Supervision: B.L.A.; Project administration: B.L.A.; Funding acquisition: M.L.E.-A., B.L.A.

Funding
This work was supported by the National Science Foundation Graduate Research Fellowship Program [DGE1256260 to M.L.E.-A.], Bradley M. Patten Fellowship [Department of Cell and Developmental Biology, Medical School, University of Michigan to M.L.E.-A.], Rackham Merit Fellowship [Horace H. Rackham School of Graduate Studies, University of Michigan to M.L.E.-A.], and the Center for Organogenesis T32 Training Grant [National Institutes of Health T32 HD007505 to M.L.E.-A.]. This work was also supported by the National Institutes of Health [R01 DC014428, R01 CA198074, R01 GM118751 to B.L.A.]. Research reported in this publication was also supported by the University of Michigan Comprehensive Cancer Center Support Grant [P30 CA046592] by the use of the following Cancer Center Shared Resource: Cell and Tissue Imaging. Deposited in PMC for release after 12 months.

Supplementary information
Supplementary information available online at
https://dev.biologists.org/lookup/doi/10.1242/dev.189076.supplemental

Peer review history
The peer review history is available online at
https://dev.biologists.org/lookup/doi/10.1242/dev.189076.reviewer-comments.pdf

References
Allen, B. L., Tenzen, T. and McMahon, A. P. (2007). The Hedgehog-binding proteins Gas1 and Cdo cooperate to positively regulate Shh signaling during mouse development. *Genes Dev.* **21**, 1244-1257. doi:10.1101/gad.1543607

Allen, B. L., Song, J. Y., Izzi, L., Althaus, I. W., Kang, J.-S., Charron, F., Krauss, R. S. and McMahon, A. P. (2011). Overlapping roles and collective requirement for the coreceptors GAS1, CDO, and BOC in SHH pathway function. *Dev. Cell* **20**, 775-787. doi:10.1016/j.devcel.2011.04.018

Aoto, K., Shikata, Y., Imai, H., Matsumaru, D., Tokunaga, T., Shioda, S., Yamada, G. and Motoyama, J. (2009). Mouse Shh is required for prechordal plate maintenance during brain and craniofacial morphogenesis. *Dev. Biol.* **327**, 106-120. doi:10.1016/j.ydbio.2008.11.022

Bae, G.-U., Domené, S., Roessler, E., Schachter, K., Kang, J.-S., Muenke, M. and Krauss, R. S. (2011). Mutations in CDON, encoding a hedgehog receptor, result in holoprosencephaly and defective interactions with other hedgehog receptors. *Am. J. Hum. Genet.* **89**, 231-240. doi:10.1016/j.ajhg.2011.07.001

Beachy, P. A., Hymowitz, S. G., Lazarus, R. A., Leahy, D. J. and Siebold, C. (2010). Interactions between Hedgehog proteins and their binding partners come into view. *Genes Dev.* **24**, 2001-2012. doi:10.1101/gad.1951710

Bergeron, S. A., Tyurina, O. V., Miller, E., Bagas, A. and Karlstrom, R. O. (2011). Brother of cdo (umleitung) is cell-autonomously required for Hedgehog-mediated ventral CNS patterning in the zebrafish. *Development* **138**, 75-85. doi:10.1242/dev.057950

Briscoe, J. and Thérond, P. P. (2013). The mechanisms of Hedgehog signalling and its roles in development and disease. *Nat. Rev. Mol. Cell Biol.* **14**, 416-429. doi:10.1038/nrm3598

Briscoe, J., Pierani, A., Jessell, T. M. and Ericson, J. (2000). A homeodomain protein code specifies progenitor cell identity and neuronal fate in the ventral neural tube. *Cell* **101**, 435-445. doi:10.1016/S0092-8674(00)80853-3

Brugmann, S. A., Allen, N. C., James, A. W., Mekonnen, Z., Madan, E. and Helms, J. A. (2010). A primary cilia-dependent etiology for midline facial disorders. *Hum. Mol. Genet.* **19**, 1577-1592. doi:10.1093/hmg/ddq030

Cabrera, J. R., Sanchez-Pulido, L., Rojas, A. M., Valencia, A., Mañes, S., Naranjo, J. R. and Mellström, B. (2006). Gas1 is related to the glial cell-derived neurotrophic factor family receptors alpha and regulates Ret signaling. *J. Biol. Chem.* **281**, 14330-14339. doi:10.1074/jbc.M509572200

Cardozo, M. J., Sánchez-Arrones, L., Sandonis, A., Sánchez-Camacho, C., Gestri, G., Wilson, S. W., Guerrero, I. and Bovolenta, P. (2014). Cdon acts as a Hedgehog decoy receptor during proximal-distal patterning of the optic vesicle. *Nat. Commun.* **5**, 4272. doi:10.1038/ncomms5272

Chiang, C., Litingtung, Y., Lee, E., Young, K. E., Corden, J. L., Westphal, H. and Beachy, P. A. (1996). Cyclopia and defective axial patterning in mice lacking Sonic hedgehog gene function. *Nature* **383**, 407-413. doi:10.1038/383407a0

Cobourne, M. T., Miletich, I. and Sharpe, P. T. (2004). Restriction of sonic hedgehog signalling during early tooth development. *Development* **131**, 2875-2885. doi:10.1242/dev.01163

Cole, F. and Krauss, R. S. (2003). Microform holoprosencephaly in mice that lack the Ig superfamily member Cdon. *Curr. Biol.* **13**, 411-415. doi:10.1016/S0960-9822(03)00088-5

Cordero, D., Marcucio, R., Hu, D., Gaffield, W., Tapadia, M. and Helms, J. A. (2004). Temporal perturbations in sonic hedgehog signaling elicit the spectrum of holoprosencephaly phenotypes. *J. Clin. Invest.* **114**, 485-494. doi:10.1172/JCI200419596

Dai, P., Akimaru, H., Tanaka, Y., Maekawa, T., Nakafuku, M. and Ishii, S. (1999). Sonic Hedgehog-induced activation of the Gli1 promoter is mediated by GLI3. *J. Biol. Chem.* **274**, 8143-8152. doi:10.1074/jbc.274.12.8143

Dessaud, E., McMahon, A. P. and Briscoe, J. (2008). Pattern formation in the vertebrate neural tube: a sonic hedgehog morphogen-regulated transcriptional network. *Development* **135**, 2489-2503. doi:10.1242/dev.009324

Ho, T.-V., Iwata, J., Ho, H. A., Grimes, W. C., Park, S., Sanchez-Lara, P. A. and Chai, Y. (2015). Integration of comprehensive 3D microCT and signaling analysis reveals differential regulatory mechanisms of craniofacial bone development. *Dev. Biol.* **400**, 180-190. doi:10.1016/j.ydbio.2015.02.010

Holtz, A. M., Peterson, K. A., Nishi, Y., Morin, S., Song, J. Y., Charron, F., McMahon, A. P. and Allen, B. L. (2013). Essential role for ligand-dependent feedback antagonism of vertebrate hedgehog signaling by PTCH1, PTCH2 and HHIP1 during neural patterning. *Development* **140**, 3423-3434. doi:10.1242/dev.095083

Hong, M. and Krauss, R. S. (2018). Modeling the complex etiology of holoprosencephaly in mice. *Am. J. Med. Genet. C Semin. Med. Genet.* **178**, 140-150. doi:10.1002/ajmg.c.31611

Hong, M., Srivastava, K., Kim, S., Allen, B. L., Leahy, D. J., Hu, P., Roessler, E., Krauss, R. S. and Muenke, M. (2017). BOC is a modifier gene in holoprosencephaly. *Hum. Mutat.* **38**, 1464-1470. doi:10.1002/humu.23286

Hu, D. and Helms, J. A. (1999). The role of sonic hedgehog in normal and abnormal craniofacial morphogenesis. *Development* **126**, 4873-4884.

Hui, C.-C. and Angers, S. (2011). Gli proteins in development and disease. *Annu. Rev. Cell Dev. Biol.* **27**, 513-537. doi:10.1146/annurev-cellbio-092910-154048

Izzi, L., Lévesque, M., Morin, S., Laniel, D., Wilkes, B. C., Mille, F., Krauss, R. S., McMahon, A. P., Allen, B. L. and Charron, F. (2011). Boc and Gas1 each form distinct Shh receptor complexes with Ptch1 and are required for Shh-mediated cell proliferation. *Dev. Cell* **20**, 788-801. doi:10.1016/j.devcel.2011.04.017

Jeong, J., Mao, J., Tenzen, T., Kottmann, A. H. and McMahon, A. P. (2004). Hedgehog signaling in the neural crest cells regulates the patterning and growth of facial primordia. *Genes Dev.* **18**, 937-951. doi:10.1101/gad.1190304

Jiang, R., Bush, J. O. and Lidral, A. C. (2006). Development of the upper lip: morphogenetic and molecular mechanisms. *Dev. Dyn.* **235**, 1152-1166. doi:10.1002/dvdy.20646

Kang, J.-S., Gao, M., Feinleib, J. L., Cotter, P. D., Guadagno, S. N. and Krauss, R. S. (1997). CDO: an oncogene-, serum-, and anchorage-regulated member of the Ig/fibronectin type III repeat family. *J. Cell Biol.* **138**, 203-213. doi:10.1083/jcb.138.1.203

Kang, J.-S., Mulieri, P. J., Hu, Y., Taliana, L. and Krauss, R. S. (2002). BOC, an Ig superfamily member, associates with CDO to positively regulate myogenic differentiation. *EMBO J.* **21**, 114-124. doi:10.1093/emboj/21.1.114

Krauss, R. S. (2007). Holoprosencephaly: new models, new insights. *Expert Rev. Mol. Med.* **9**, 1-17. doi:10.1017/S1462399407000440

Kuwajima, T., Sitko, A. A., Bhansali, P., Jurgens, C., Guido, W. and Mason, C. (2013). ClearT: a detergent- and solvent-free clearing method for neuronal and non-neuronal tissue. *Development* **140**, 1364-1368. doi:10.1242/dev.091844

Lee, C. S., Buttitta, L. and Fan, C.-M. (2001). Evidence that the WNT-inducible growth arrest-specific gene 1 encodes an antagonist of sonic hedgehog signaling in the somite. *Proc. Natl. Acad. Sci. USA* **98**, 11347-11352. doi:10.1073/pnas.201418298

Lum, L., Yao, S., Mozer, B., Rovescalli, A., Von Kessler, D., Nirenberg, M. and Beachy, P. A. (2003). Identification of Hedgehog pathway components by RNAi in Drosophila cultured cells. *Science* **299**, 2039-2045. doi:10.1126/science.1081403

Makihara, S., Morin, S., Ferent, J., Cote, J. F., Yam, P. T. and Charron, F. (2018). Polarized dock activity drives shh-mediated axon guidance. *Dev. Cell* **46**, 410-425.e417. doi:10.1016/j.devcel.2018.07.007

Marcucio, R. S., Cordero, D. R., Hu, D. and Helms, J. A. (2005). Molecular interactions coordinating the development of the forebrain and face. *Dev. Biol.* **284**, 48-61. doi:10.1016/j.ydbio.2005.04.030

Marigo, V., Davey, R. A., Zuo, Y., Cunningham, J. M. and Tabin, C. J. (1996). Biochemical evidence that patched is the Hedgehog receptor. *Nature* **384**, 176-179. doi:10.1038/384176a0

Martinelli, D. C. and Fan, C.-M. (2007). Gas1 extends the range of Hedgehog action by facilitating its signaling. *Genes Dev.* **21**, 1231-1243. doi:10.1101/gad.1546307

McLellan, J. S., Zheng, X., Hauk, G., Ghirlando, R., Beachy, P. A. and Leahy, D. J. (2008). The mode of Hedgehog binding to Ihog homologues is not conserved across different phyla. *Nature* **455**, 979-983. doi:10.1038/nature07358

McMahon, A. P., Ingham, P. W. and Tabin, C. J. (2003). Developmental roles and clinical significance of hedgehog signaling. *Curr. Top. Dev. Biol.* **53**, 1-114. doi:10.1016/S0070-2153(03)53002-2

Muenke, M. and Beachy, P. A. (2000). Genetics of ventral forebrain development and holoprosencephaly. *Curr. Opin. Genet. Dev.* **10**, 262-269. doi:10.1016/S0959-437X(00)00084-8

Ohazama, A., Haycraft, C. J., Seppala, M., Blackburn, J., Ghafoor, S., Cobourne, M., Martinelli, D. C., Fan, C.-M., Peterkova, R., Lesot, H. et al. (2009). Primary cilia regulate Shh activity in the control of molar tooth number. *Development* **136**, 897-903. doi:10.1242/dev.027979

Okada, A., Charron, F., Morin, S., Shin, D. S., Wong, K., Fabre, P. J., Tessier-Lavigne, M. and McConnell, S. K. (2006). Boc is a receptor for sonic hedgehog in the guidance of commissural axons. *Nature* **444**, 369-373. doi:10.1038/nature05246

Pabst, O., Herbrand, H., Takuma, N. and Arnold, H.-H. (2000). NKX2 gene expression in neuroectoderm but not in mesendodermally derived structures depends on sonic hedgehog in mouse embryos. *Dev. Genes Evol.* **210**, 47-50. doi:10.1007/PL00008188

Ribeiro, L. A., Quiezi, R. G., Nascimento, A., Bertolacini, C. P. and Richieri-Costa, A. (2010). Holoprosencephaly and holoprosencephaly-like phenotype and GAS1 DNA sequence changes: Report of four Brazilian patients. *Am. J. Med. Genet. A* **152A**, 1688-1694. doi:10.1002/ajmg.a.33466

Roessler, E. and Muenke, M. (2010). The molecular genetics of holoprosencephaly. *Am. J. Med. Genet. C Semin. Med. Genet.* **154C**, 52-61. doi:10.1002/ajmg.c.30236

Roessler, E., El-Jaick, K. B., Dubourg, C., Vélez, J. I., Solomon, B. D., Pineda-Álvarez, D. E., Lacbawan, F., Zhou, N., Ouspenskaia, M., Paulussen, A. et al. (2009). The mutational spectrum of holoprosencephaly-associated changes within the SHH gene in humans predicts loss-of-function through either key structural alterations of the ligand or its altered synthesis. *Hum. Mutat.* **30**, E921-E935. doi:10.1002/humu.21090

Rubenstein, J. L. and Beachy, P. A. (1998). Patterning of the embryonic forebrain. *Curr. Opin. Neurobiol.* **8**, 18-26. doi:10.1016/S0959-4388(98)80004-4

Schachter, K. A. and Krauss, R. S. (2008). Murine models of holoprosencephaly. *Curr. Top. Dev. Biol.* 84, 139-170. doi:10.1016/S0070-2153(08)00603-0

Schneider, C. A., Rasband, W. S. and Eliceiri, K. W. (2012). NIH Image to ImageJ: 25 years of image analysis. *Nat. Methods* **9**, 671-675. doi:10.1038/nmeth.2089

Seppala, M., Depew, M. J., Martinelli, D. C., Fan, C.-M., Sharpe, P. T. and Cobourne, M. T. (2007). Gas1 is a modifier for holoprosencephaly and genetically interacts with sonic hedgehog. *J. Clin. Invest.* **117**, 1575-1584. doi:10.1172/JCI32032

Seppala, M., Xavier, G. M., Fan, C.-M. and Cobourne, M. T. (2014). Boc modifies the spectrum of holoprosencephaly in the absence of Gas1 function. *Biol. Open* **3**, 728-740. doi:10.1242/bio.20147989

Tenzen, T., Allen, B. L., Cole, F., Kang, J.-S., Krauss, R. S. and McMahon, A. P. (2006). The cell surface membrane proteins Cdo and Boc are components and targets of the Hedgehog signaling pathway and feedback network in mice. *Dev. Cell* **10**, 647-656. doi:10.1016/j.devcel.2006.04.004

Vuong, T. A., Leem, Y.-E., Kim, B.-G., Cho, H., Lee, S.-J., Bae, G.-U. and Kang, J.-S. (2017). A Sonic hedgehog coreceptor, BOC regulates neuronal differentiation and neurite outgrowth via interaction with ABL and JNK activation. *Cell. Signal.* **30**, 30-40. doi:10.1016/j.cellsig.2016.11.013

Wilkinson, D. G. (1992). *In Situ Hybridization: a Practical Approach*. Oxford; New York: IRL Press at Oxford University Press.

Xavier, G. M., Seppala, M., Barrell, W., Birjandi, A. A., Geoghegan, F. and Cobourne, M. T. (2016a). Hedgehog receptor function during craniofacial development. *Dev. Biol.* **415**, 198-215. doi:10.1016/j.ydbio.2016.02.009

Xavier, G. M., Seppala, M., Papageorgiou, S. N., Fan, C.-M. and Cobourne, M. T. (2016b). Genetic interactions between the hedgehog co-receptors Gas1 and Boc regulate cell proliferation during murine palatogenesis. *Oncotarget* **7**, 79233-79246. doi:10.18632/oncotarget.13011

Xie, J., Murone, M., Luoh, S.-M., Ryan, A., Gu, Q., Zhang, C., Bonifas, J. M., Lam, C.-W., Hynes, M., Goddard, A. et al. (1998). Activating Smoothened mutations in sporadic basal-cell carcinoma. *Nature* **391**, 90-92. doi:10.1038/34201

Xu, J., Liu, H., Lan, Y., Adam, M., Clouthier, D. E., Potter, S. and Jiang, R. (2019). Hedgehog signaling patterns the oral-aboral axis of the mandibular arch. *Elife* **8**, e40315. doi:10.7554/eLife.40315

Yao, S., Lum, L. and Beachy, P. (2006). The ihog cell-surface proteins bind Hedgehog and mediate pathway activation. *Cell* **125**, 343-357. doi:10.1016/j.cell.2006.02.040

Zhang, W., Kang, J.-S., Cole, F., Yi, M.-J. and Krauss, R. S. (2006). Cdo functions at multiple points in the Sonic Hedgehog pathway, and Cdo-deficient mice accurately model human holoprosencephaly. *Dev. Cell* **10**, 657-665. doi:10.1016/j.devcel.2006.04.005

Zhang, W., Hong, M., Bae, G.-U., Kang, J.-S. and Krauss, R. S. (2011). Boc modifies the holoprosencephaly spectrum of Cdo mutant mice. *Dis. Model. Mech.* **4**, 368-380. doi:10.1242/dmm.005744

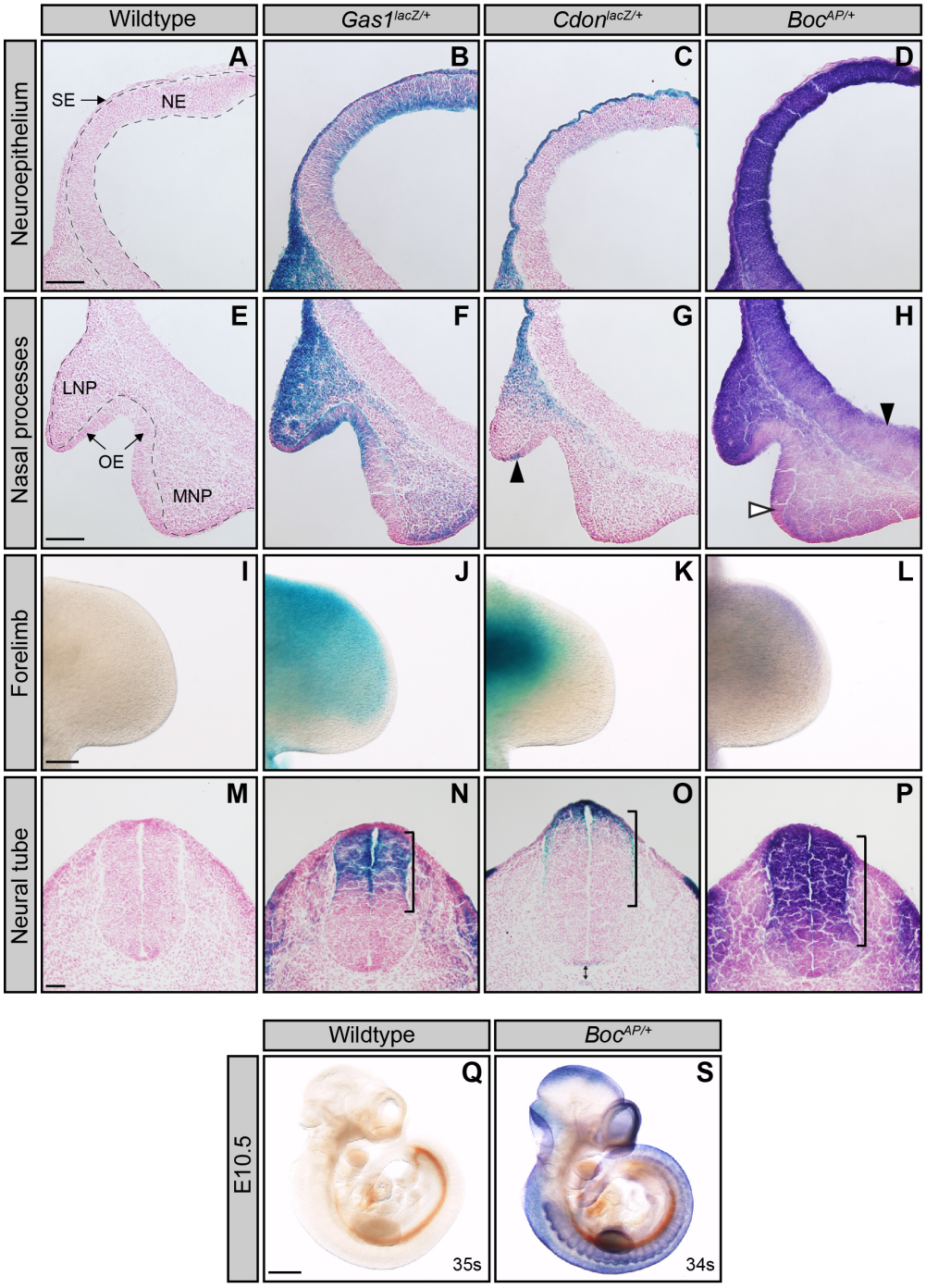

Figure S1. *Gas1, Cdon* and *Boc* are differentially expressed across multiple HH-responsive tissues.

Analysis of HH co-receptor expression using *lacZ* (*Gas1*, *Cdon*) and *hPLAP* (*Boc*) reporter alleles in HH-responsive tissues (A-P). High magnification pictures of coronal sections of E10.5 forebrains (A-H; cf. Fig.1Q-T), from wildtype (A, E), *Gas1*$^{lacZ/+}$ (B, F), *Cdon*$^{lacZ/+}$ (C, G), and *Boc*$^{AP/+}$ (D, H) embryos are shown. E10.5 forebrain neuroepithelia (A-D) and nasal processes (E-H). Arrowhead in (G) denotes a subset of cells expressing *Cdon* in the olfactory epithelium. Black arrowhead in (H) identifies the extended ventral expression of *Boc* closer to the telencephalon source of *Shh* expression. White arrowhead in (H) denotes *Boc* expression in the

olfactory epithelium. Whole mount X-Gal and Alkaline Phosphatase staining of E10.5 forelimb buds (I-L) from wildtype (I), *Gas1*$^{lacZ/+}$ (J), *Cdon*$^{lacZ/+}$ (K), and *Boc*$^{AP/+}$ (L) embryos. Transverse sections of E10.5 neural tubes (M-P) from wildtype (M), *Gas1*$^{lacZ/+}$ (N), *Cdon*$^{lacZ/+}$ (O), and *Boc*$^{AP/+}$ (P) embryos. Black brackets denote the expression domain of the HH co-receptors in the neural tube. Double-headed arrow in (O) indicates *Cdon* expression in the floor plate and notochord. Heat inactivation of endogenous alkaline phosphatase at E10.5 in wildtype (Q) and *Boc*$^{AP/+}$ (S) animals demonstrates the specificity of alkaline phosphatase staining. Somite number (s) is indicated in the lower right corner (Q-S). Scale bars, (A-H) 100µm, (I-L) 200µm, (M-P) 50µm, (Q-S) 500µm. Abbreviations: surface ectoderm (SE), neuroepithelium (NE), lateral nasal process (LNP), medial nasal process (MNP), olfactory epithelium (OE).

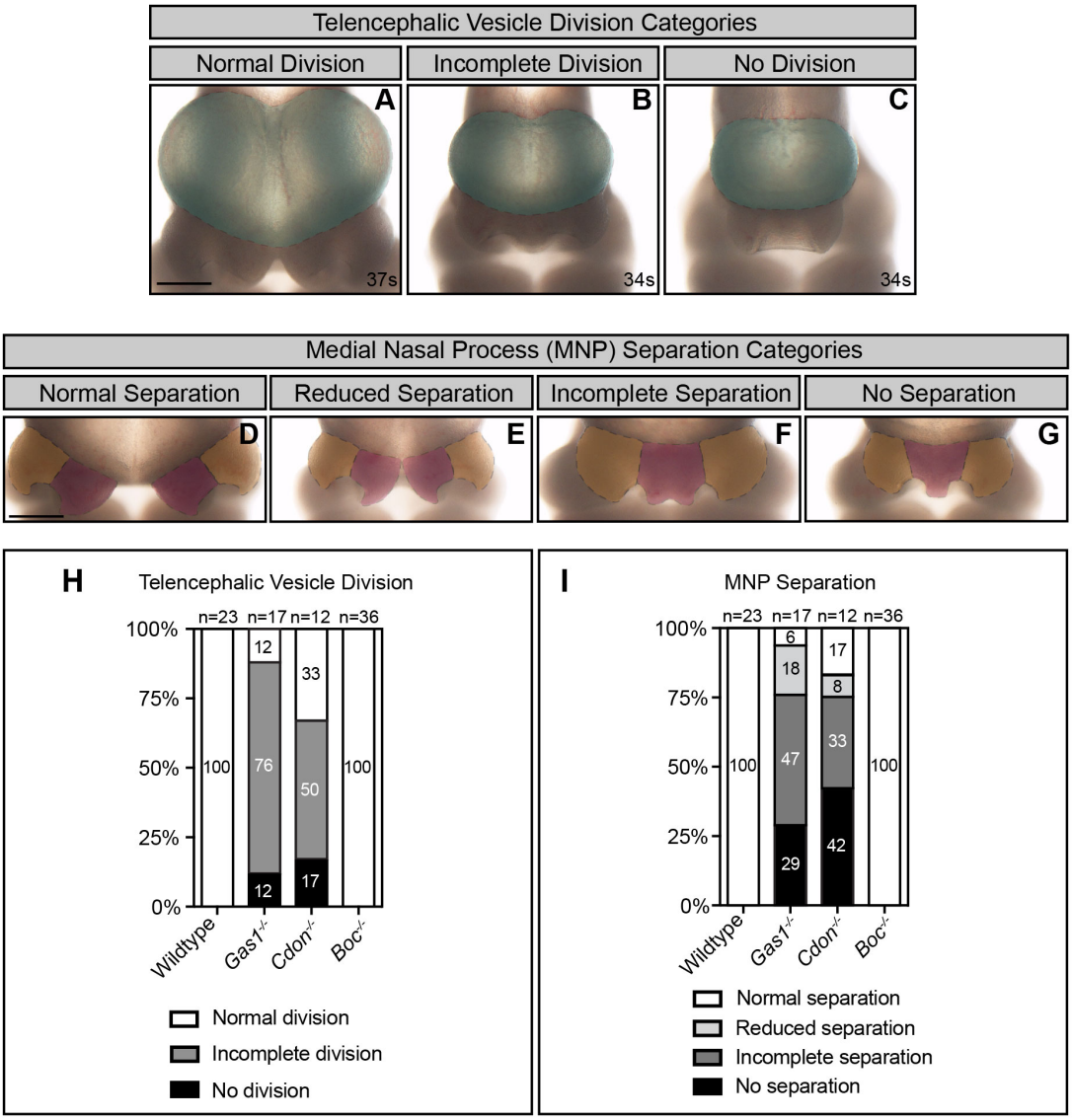

Figure S2. Telencephalic vesicle division and MNP separation in *Gas1*, *Cdon* and *Boc* mutants.

En face view of E10.5 embryos (A-C). The telencephalic vesicles are pseudocolored in green and surrounded by a dotted line. Telencephalic vesicle division classification categories: normal division (A), incomplete division (B), no division (C). Midface view of E10.5 embryos (D-G). The lateral and medial nasal processes are pseudocolored in orange and red, respectively, and are surrounded by a dotted line. Medial nasal process (MNP) classification categories: normal separation (D), reduced separation (E), incomplete separation (F), and no separation (G). Scale bars (A, D), 500µm. Telencephalic vesicle (TV) division frequency in E10.5 wildtype (n=23), *Gas1*$^{-/-}$ (n=17), *Cdon*$^{-/-}$ (n=12), and *Boc*$^{-/-}$ (n=36) embryos (H). Medial nasal process (MNP) separation frequency in E10.5 wildtype (n=23), *Gas1*$^{-/-}$ (n=17), *Cdon*$^{-/-}$ (n=12), and *Boc*$^{-/-}$ (n=36) embryos (I).

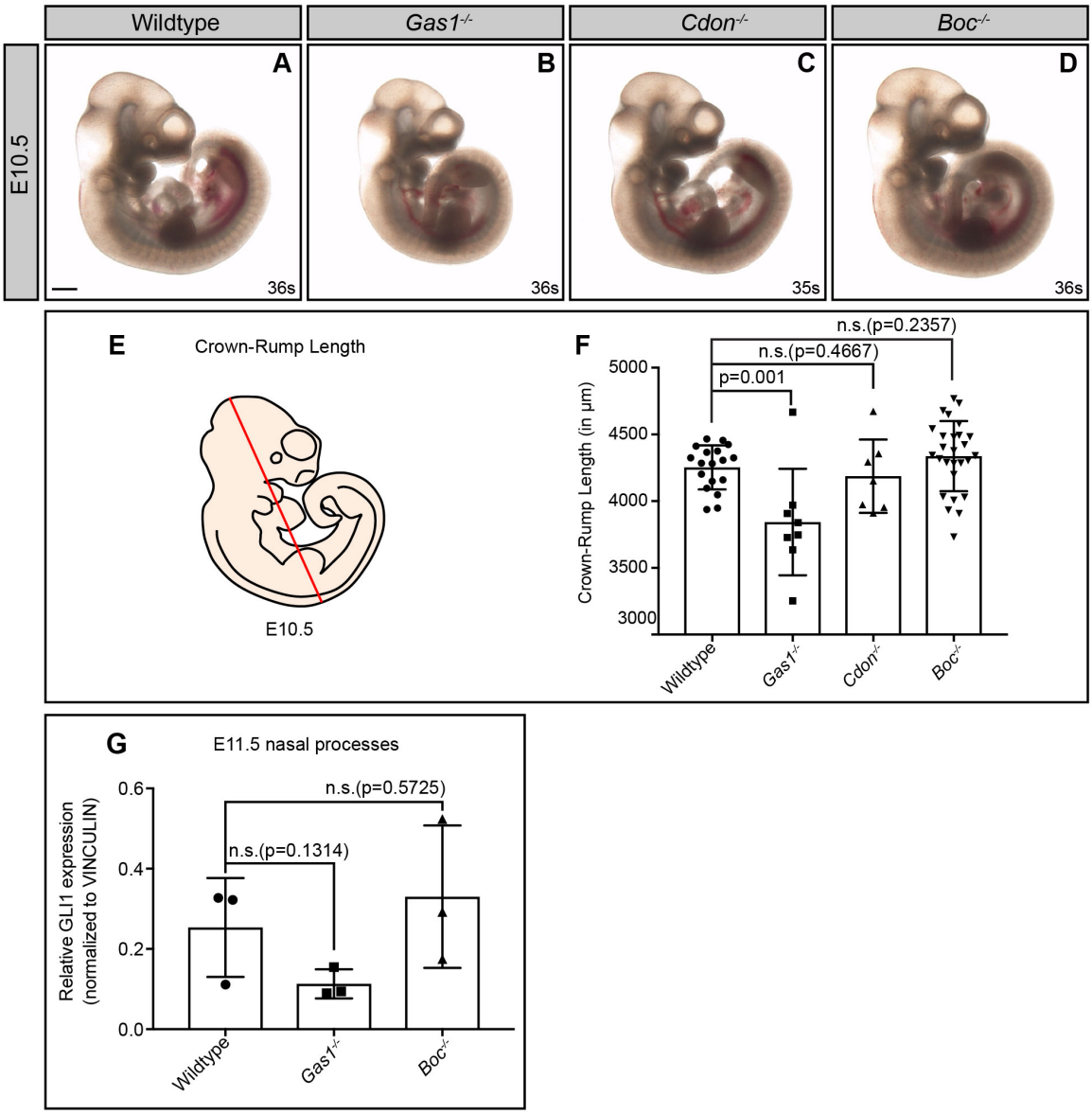

Figure S3. Reduced embryo size in E10.5 *Gas1*, but not *Cdon* or *Boc*, mutant embryos. Sagittal views of E10.5 wildtype (A), *Gas1*$^{-/-}$ (B), *Cdon*$^{-/-}$(C), and *Boc*$^{-/-}$(D) embryos. Scale bar (A), 500 µm. Schematic sagittal view of an E10.5 mouse embryo (E); the red diagonal line denotes crown-rump length. Crown-rump length quantitation of E10.5 wildtype (n= 18), *Gas1*$^{-/-}$ (n=8), *Cdon*$^{-/-}$ (n=7), *Boc*$^{-/-}$ (n=27) embryos (F). Quantitation of GLI1 levels in nasal processes isolated from E11.5 wildtype (n=3), *Gas1*$^{-/-}$ (n=3) and *Boc*$^{-/-}$ (n=3) embryos (G). Data are mean ±s.d. P-values were determined by a two-tailed Student's *t*-test. The Bonferroni correction was employed to account for multiple comparisons in each dataset; (F) non-significant (n.s.; $p>0.0166$), significant ($p\leq0.0166$) and (G) non-significant (n.s.; $p>0.0250$), significant ($p\leq0.0250$).

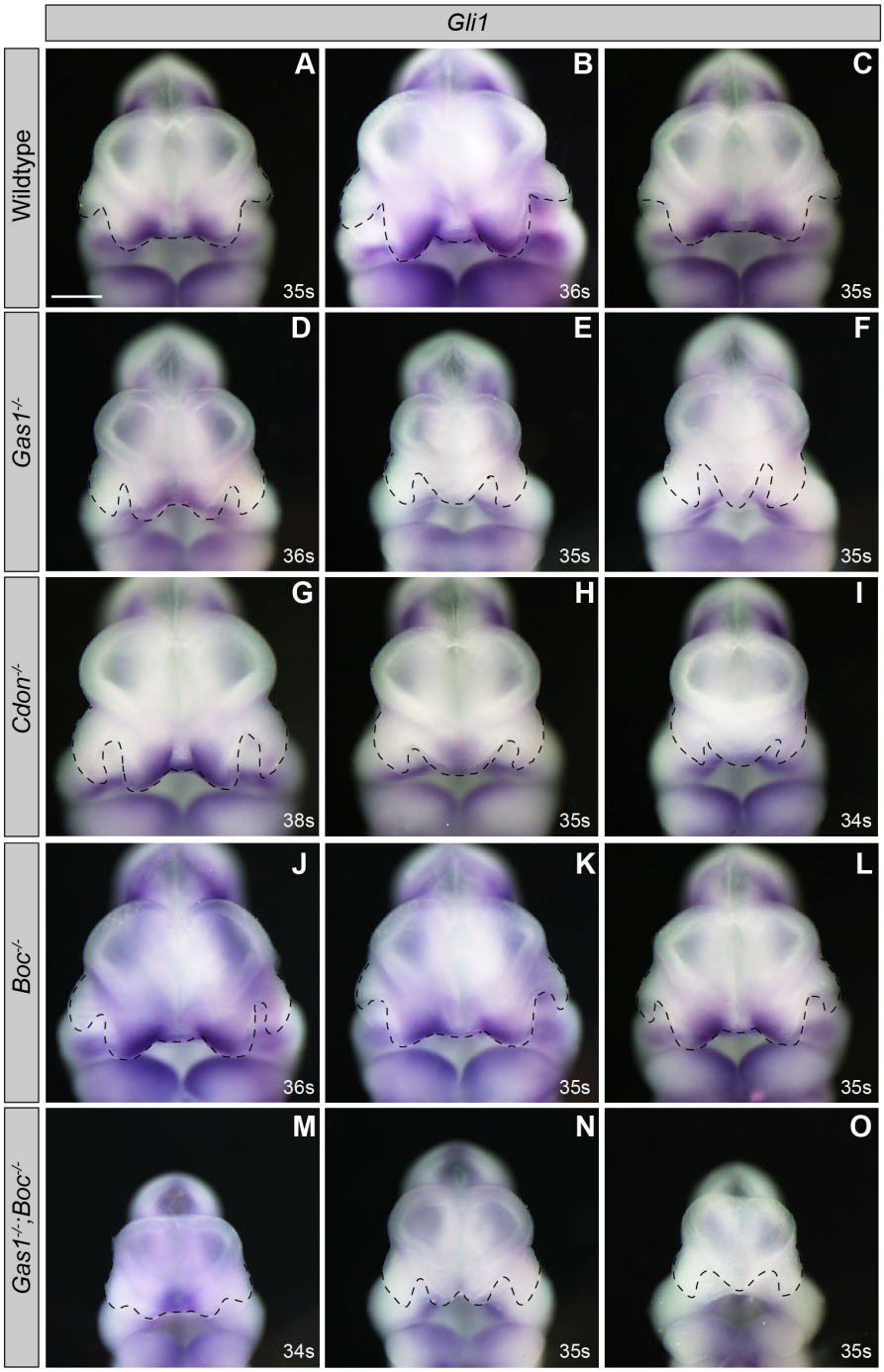

Figure S4. The spectrum of HPE phenotypes correlates with changes in *Gli1* expression. *In situ* hybridization detection of *Gli1* expression in E10.5 forebrains (A-O). *En face* views of E10.5 forebrains from wildtype (A-C), *Gas1*$^{-/-}$ (D-F), *Cdon*$^{-/-}$ (G-I), *Boc*$^{-/-}$ (J-L) and *Gas1*$^{-/-}$*;Boc*$^{-/-}$ (M-O) embryos are shown. Somite number (s) is indicated in the lower right corner of each panel. Black dotted lines outline nasal processes. Notice that as the HPE phenotypes worsen (from left to right) in *Gas1* and *Cdon* mutants, the expression of *Gli1* in the MNP is lost. *Boc* mutants display equal levels of *Gli1* in the MNP and do not display any gross craniofacial defects. *Gas1;Boc* double mutants with ameliorated craniofacial defects (from left to right) maintain *Gli1* expression in the MNP, while *Gli1* expression is lost in mutants that display severe craniofacial defects. Scale bars (A-O), 500 μm.

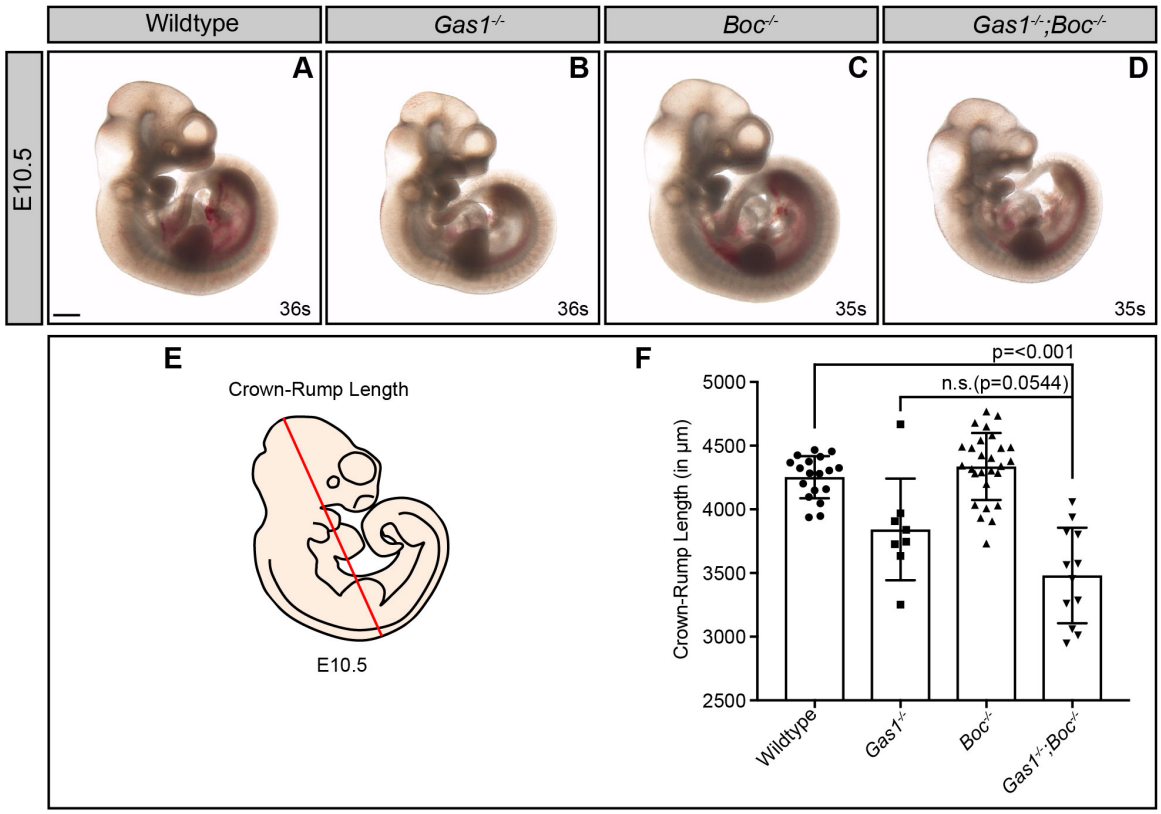

Figure S5. Reduced Crown-Rump Length in E10.5 *Gas1;Boc* double mutant embryos. Sagittal view of E10.5 wildtype (A), *Gas1*$^{-/-}$ (B), *Boc*$^{-/-}$ (C), and *Gas1*$^{-/-}$*;Boc*$^{-/-}$ (D) embryos. Schematic sagittal view of an E10.5 mouse embryo; the red diagonal line denotes the crown-rump length (E). Crown-rump length quantitation in wildtype (n= 18), *Gas1*$^{-/-}$ (n=8), *Boc*$^{-/-}$ (n=27), and *Gas1*$^{-/-}$*;Boc*$^{-/-}$ (n=12) embryos (F). Scale bar in A, 500µm. Data are mean±s.d. P-values were determined by a two-tailed Student's *t*-test. The Bonferroni correction was employed to account for multiple comparisons in each dataset; (F) non-significant (n.s.; $p>0.0250$), significant ($p\leq0.0250$).

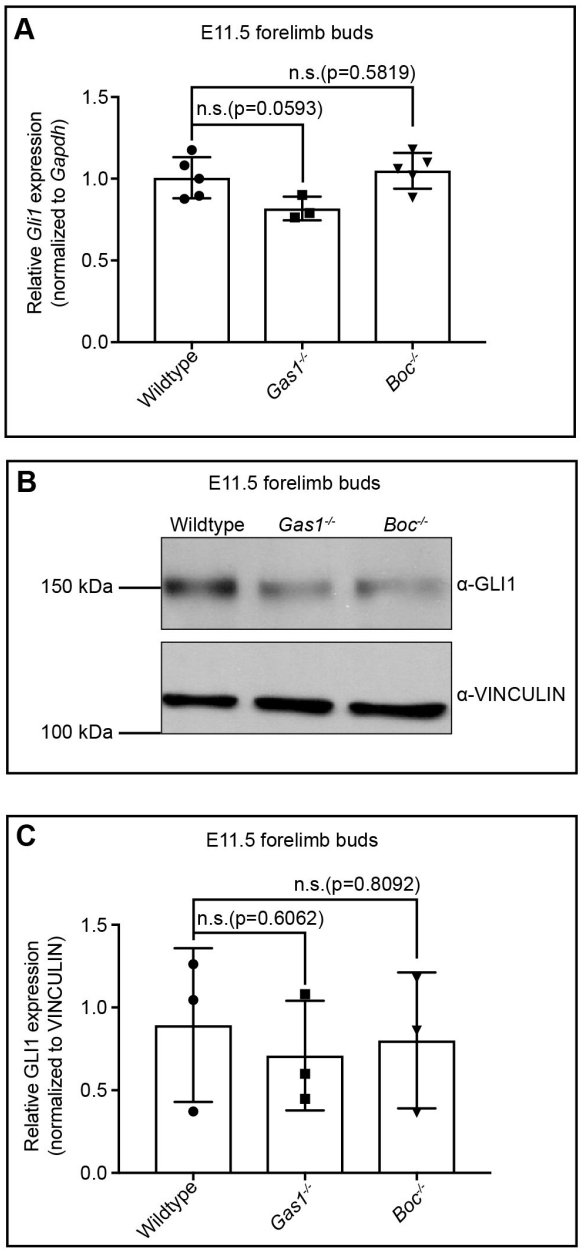

Figure S6. *Gli1* mRNA and protein levels in E10.5 *Gas1* and *Boc* mutant forelimb buds. Relative expression of *Gli1* by qRT-PCR in forelimb buds (A) of E11.5 wildtype (n=5), *Gas1*$^{-/-}$ (n=3) and *Boc*$^{-/-}$ (n=5) embryos normalized to *Gapdh.* Biological replicates were analyzed in triplicate. Western blot analysis of GLI1 endogenous protein in forelimb buds (B). Anti-VINCULIN was used as loading control, three biological replicates were analyzed. Quantitation of GLI1 levels in forelimb buds (C) of E11.5 wildtype (n=3), *Gas1*$^{-/-}$ (n=3) and *Boc*$^{-/-}$ (n=3) embryos. Data are mean±s.d. P-values were determined by a two-tailed Student's *t*-test. The Bonferroni correction was employed to account for multiple comparisons in each dataset; (A,C) non-significant (n.s.; p>0.0250), significant (p≤0.0250).

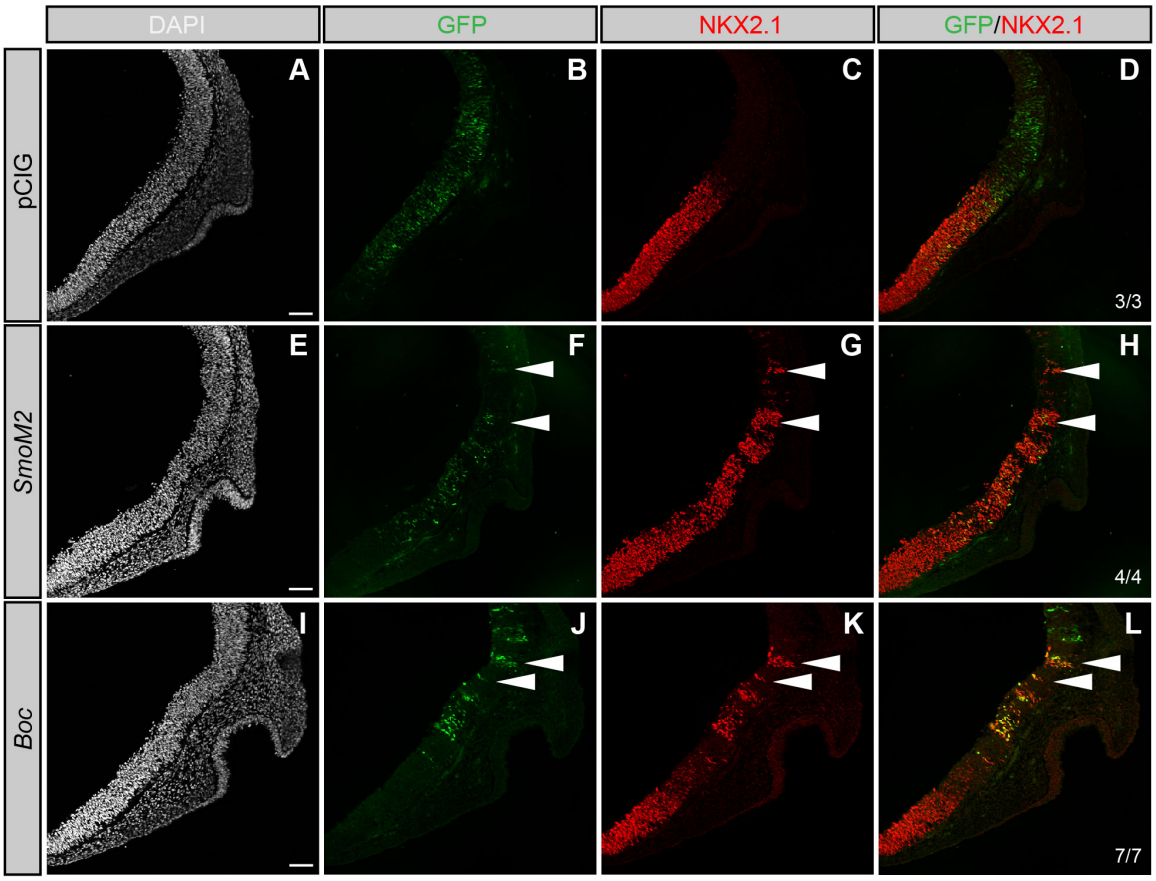

Figure S7. Boc promotes HH-dependent neural patterning in the developing chicken forebrain. Coronal sections of Hamburger-Hamilton stage 21-22 chicken forebrains electroporated with empty vector (pCIG; A-D), *SmoM2* (E-H), and *Boc* (I-L). DAPI (grayscale; A,E,I) denotes nuclei. GFP+ cells (green; B,F,J) identify electroporated cells. Antibody detection of NKX2.1 (red; C,G,K) reads out HH pathway activity. Merged images are shown in (D,H,L). The number of electroporated embryos that display ectopic NKX2.1 expression is indicated in the lower right corner (D,H,L). White arrowheads highlight ectopic NKX2.1 expression. Scale bars in A, E, and I, 50µm.

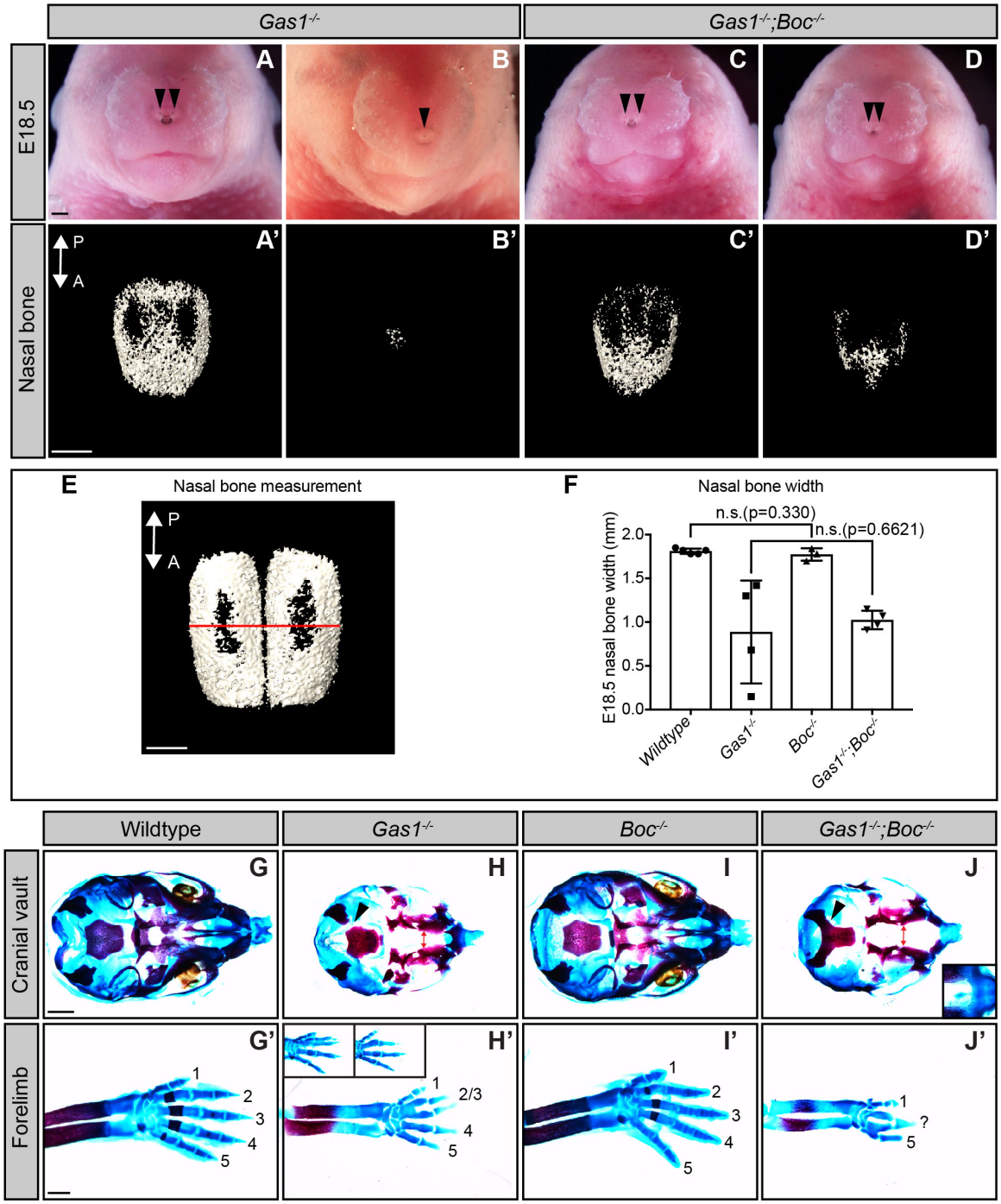

Figure S8. HPE phenotypes and digit specification defects in E18.5 *Gas1;Boc* mutant embryos.

En face view of E18.5 *Gas1*$^{-/-}$ (A,B) and *Gas1*$^{-/-}$*;Boc*$^{-/-}$ (C,D) embryos. Black arrowheads denote the nasal pits. Three dimensional reconstructions of microCT images of isolated nasal bones from E18.5 *Gas1*$^{-/-}$ (A',B') and *Gas1*$^{-/-}$*;Boc*$^{-/-}$ (C',D') embryos. A←→P specifies the anterior to posterior axis in (A'-D',E). MicroCT image of an isolated nasal bone from E18.5 wildtype embryo (E); the red horizontal line denotes the nasal bone width. Nasal bone width quantitation in wildtype (n=5), *Gas1*$^{-/-}$ (n=4), *Boc*$^{-/-}$ (n=3), and *Gas1*$^{-/-}$*;Boc*$^{-/-}$ (n=4) embryos (F). Data are

mean±s.d. P-values were determined by a two-tailed Student's *t*-test. The Bonferroni correction was employed to account for multiple comparisons in each dataset; (F) non-significant (n.s.; $p>0.0250$), significant ($p\leq0.0250$). Ventral views of E18.5 cranial vaults from wildtype (G), *Gas1*$^{-/-}$ (H), *Boc*$^{-/-}$ (I), and *Gas1*$^{-/-}$*;Boc*$^{-/-}$ (J) embryos, stained with Alcian Blue and Alizarin Red. Red double arrows denote the cleft palate in *Gas1*$^{-/-}$ and *Gas1*$^{-/-}$*;Boc*$^{-/-}$ embryos and black arrowheads mark occipital bone. Inset in (J) indicates hypoplastic premaxilla in *Gas1*$^{-/-}$*;Boc*$^{-/-}$ embryos. Forelimbs of E18.5 wildtype (G'), *Gas1*$^{-/-}$ (H'), *Boc*$^{-/-}$ (I'), and *Gas1*$^{-/-}$*;Boc*$^{-/-}$ (J') embryos, stained with Alcian Blue and Alizarin Red. Numbers denote specific digits where 1 is the most anterior and 5 is the most posterior. Insets in (H') demonstrate variable digit specification phenotypes in *Gas1*$^{-/-}$ embryos, which display either partial fusion of digits two and three (left), or the absence of either digit two or three (right). *Gas1*$^{-/-}$*;Boc*$^{-/-}$ embryos exhibit a more severe limb phenotype where only digits 1 and 5 can be clearly identified; a third, unidentified digit is labeled with a question mark (Allen et al., 2011). Scale bars (A,A',E,G',G'), 500 μm.

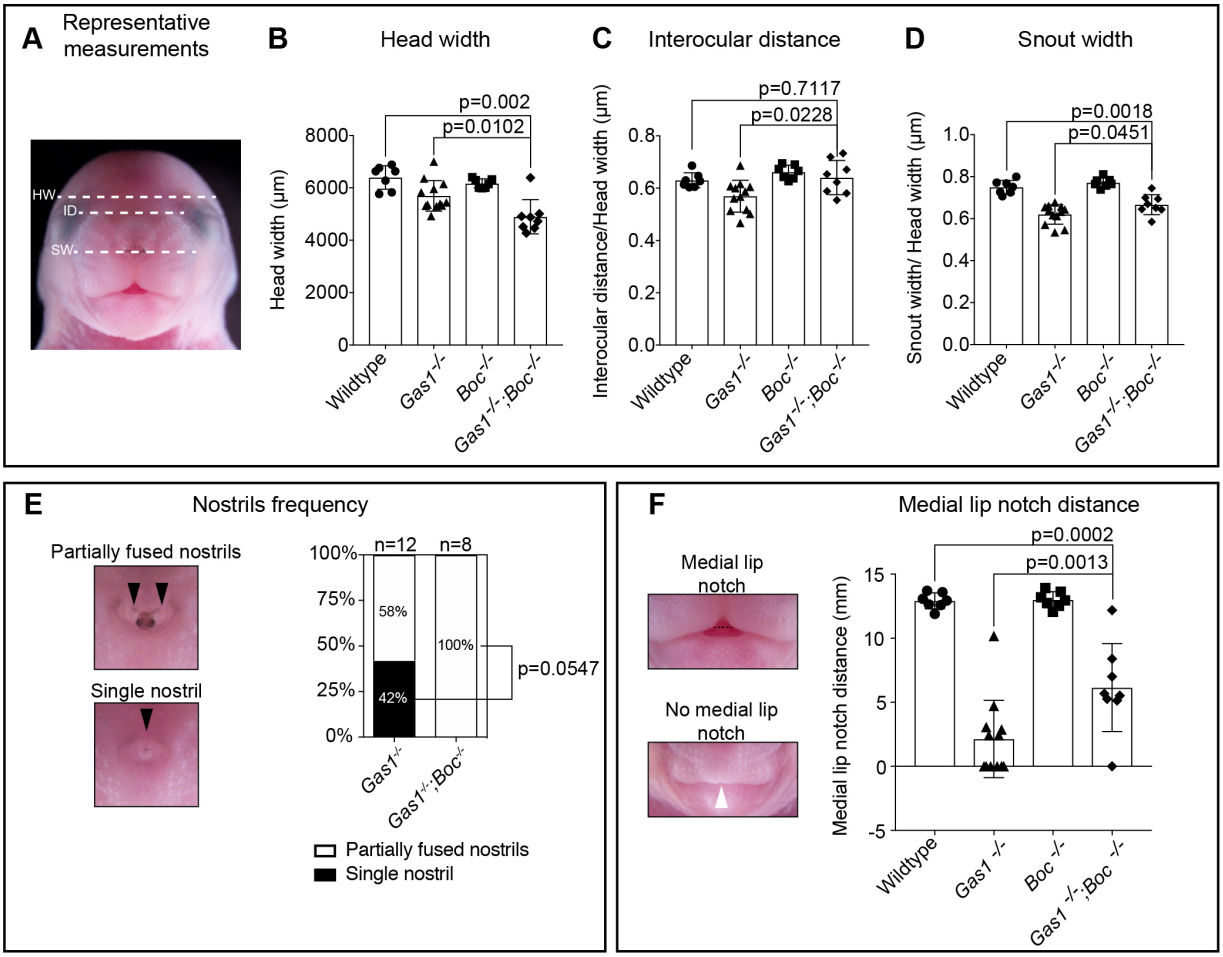

Figure S9. E18.5 *Gas1;Boc* mutants display partially ameliorated midfacial defects. Quantitation of anatomical landmarks in E18.5 embryos (A-F). Representative measurements of head width (HW), interocular distance (ID), snout width (SW) in E18.5 embryos (A). White dotted lines denote the measured distance. Head width quantitation in wildtype (n=7), *Gas1*$^{-/-}$ (n=12), *Boc*$^{-/-}$ (n=7) and *Gas1*$^{-/-}$*;Boc*$^{-/-}$ (n=8) embryos (B). Interocular distance quantitation, normalized to the head width in wildtype (n=7), *Gas1*$^{-/-}$ (n=12), *Boc*$^{-/-}$ (n=7) and *Gas1*$^{-/-}$*;Boc*$^{-/-}$ (n=8) embryos (C). Snout width quantitation, normalized to the head width in wildtype (n=7), *Gas1*$^{-/-}$ (n=12) and *Gas1*$^{-/-}$*;Boc*$^{-/-}$ (n=8) embryos (D). Nostril frequency in *Gas1*$^{-/-}$ (n=12) and *Gas1*$^{-/-}$*;Boc*$^{-/-}$ (n=8) embryos (E). Left panel, representative images of two partially fused nostrils and a single nostril. Black arrowheads denote two nostrils and a single nostril. Right panel, observed nostril frequency. Medial lip notch distance quantitation in wildtype (n=7), *Gas1*$^{-/-}$ (n=12), *Boc*$^{-/-}$ (n=7) and *Gas1*$^{-/-}$*;Boc*$^{-/-}$ (n=8) embryos (F). Left panel, representative images of medial lip notch and no medial lip notch. Right panel, medial lip notch quantitation. White arrowhead denotes the lack of a medial lip notch. Data are mean±s.d. P-values were determined by a two-tailed Student's *t*-test (B-D, F) or a Fisher's Exact test (E). The Bonferroni correction was employed to account for multiple comparisons in (B-D, F); (n.s.; p>0.0250), significant (p≤0.0250).

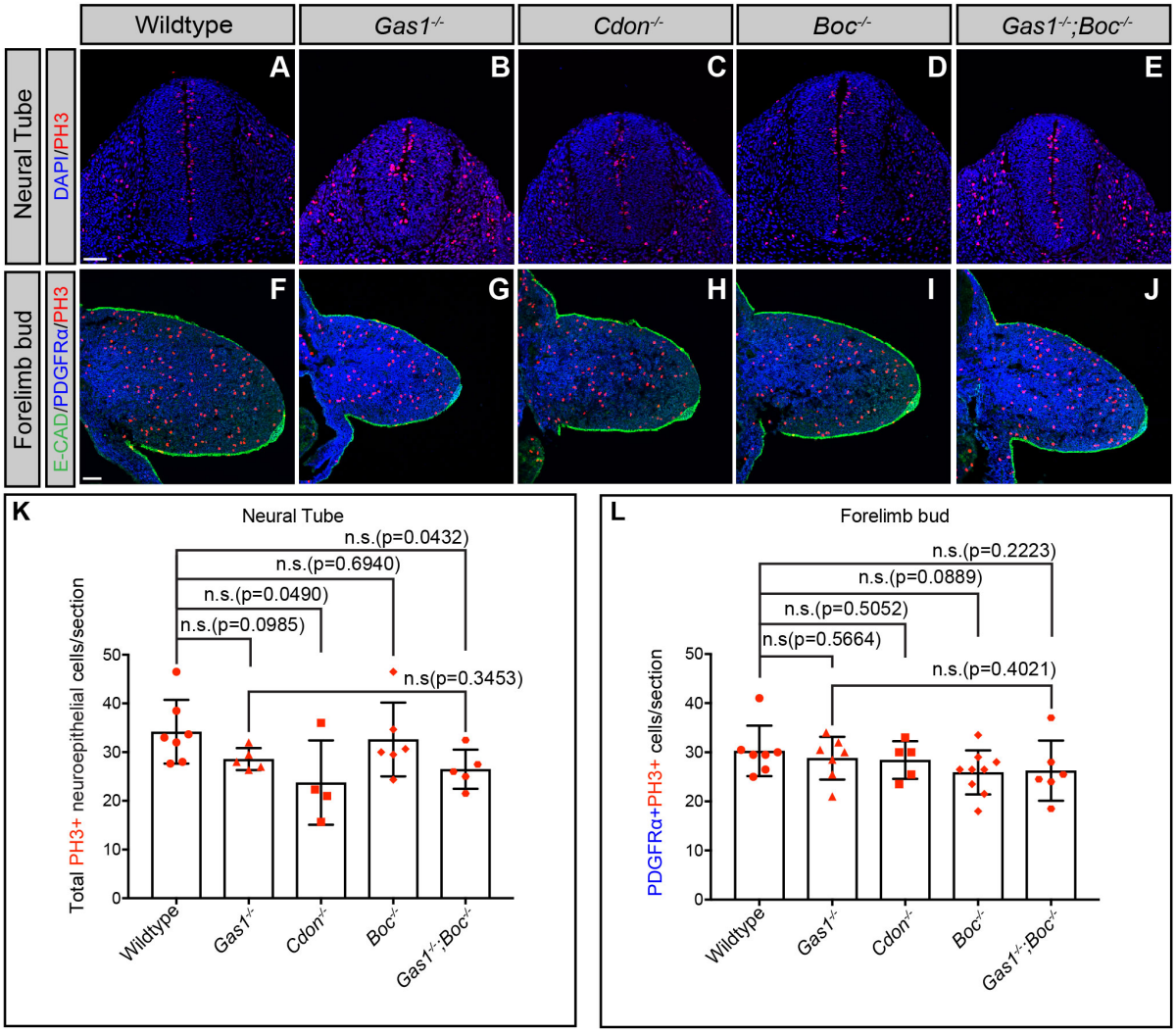

Figure S10. *Boc* does not contribute to neural tube or forelimb mesenchyme proliferation. Immunofluorescent analysis of proliferation in E10.5 neural tube (A-E) and forelimb (F-J) transverse sections from E10.5, wildtype (A,F), *Gas1*$^{-/-}$ (B,G), *Cdon*$^{-/-}$ (C,H), *Boc*$^{-/-}$ (D,I), and *Gas1*$^{-/-}$;*Boc*$^{-/-}$ (E,J) embryos. Antibody detection of E-CADHERIN (E-CAD, green, F-J), PDGFRα (blue, F-J), and phospho-histone H3 (PH3, red, A-J). Nuclei are stained with DAPI (blue, A-E). Quantitation of PH3+ cells (2 sections/embryo) in the neural tube (K) from E10.5 wildtype (n=7), *Gas1*$^{-/-}$ (n=5), *Cdon*$^{-/-}$ (n=4), *Boc*$^{-/-}$ (n=6) and *Gas1*$^{-/-}$;*Boc*$^{-/-}$ (n=5) embryos. Quantitation of PH3+ cells (2 sections/limb) in forelimb buds (L) from E10.5 wildtype (n=7), *Gas1*$^{-/-}$ (n=7), *Cdon*$^{-/-}$ (n=5), *Boc*$^{-/-}$ (n=9) and *Gas1*$^{-/-}$;*Boc*$^{-/-}$ (n=6) embryos. Data are mean±s.d. P-values were determined by a two-tailed Student's *t*-test. The Bonferroni correction was employed to account for multiple comparisons in each dataset; (K-L) non-significant (n.s.; p>0.0125), significant (p≤0.0125). Scale bars (A,F), 50 µm.

Table S1. General Reagents

Reagent	Vendor	Catalog number
Alcian Blue	Millipore Sigma	A5268
Alizarin Red	Millipore Sigma	A5533
Amersham ECL Prime Western Blotting Detection Reagent	GE Healthcare	RPN2232
Anti-Digoxigenin-Ap, Fab fragments	Roche	11 093 274 910
BM purple	Roche	11442074001
BSA	Millipore Sigma	A7906
Complete mini Protease Inhibitor Cocktail	Roche	1836153
DAPI	Thermo Fisher Scientific	D1306
EGTA	Millipore Sigma	E3889
EDTA	Thermo Fisher Scientific	S311-500
Fast green	Millipore Sigma	EM-4510
Formaldehyde	VWR	EMD-FX0410-5
Formamide	Millipore Sigma	4650-500ML
Glacial Acetic Acid	Thermo Fisher Scientific	BP2401-500
Glutaraldehyde	Millipore Sigma	G5882
Glycerol	VWR	EMGX0185-5
Goat serum	Thermo Fisher Scientific	16210064
High capacity cDNA reverse transcription kit	Applied Biosystems	4368814
Hyblot CL Autoradiography Film	Denville	E3018
Igepal (NP-40)	Millipore Sigma	I8896
Immu-mount	Thermo Fisher Scientific	9990412
Immuno-Blot PVDF membranes	Bio-Rad	162-0177
$K_3Fe(CN)_6$	Millipore Sigma	PX1455
$K_4Fe(CN)_6$	Millipore Sigma	P9387
$MgCl_2$	VWR	0288-500G
NaCl	Millipore Sigma	SX0420-3
Na deoxycholate	VWR	SX0480-2
OCT	Thermo Fisher Scientific	23730571
Paraformaldehyde	Thermo Fisher Scientific	50980489
Permount	Thermo Fisher Scientific	SP15100
Pierce BCA protein assay kit	Thermo Fisher Scientific	PI23225

Polyethyleneglycol	Millipore Sigma	91893-1L-F
Potassium hydroxide	VWR	PX1490-1
PowerUP SYBR Green Master Mix	Applied Biosystems	A25742
Proteinase K	Roche	03115836001
Quick-RNA micro prep	Zymo Research	R1055
Sheep serum	Bioworld	30611168-1
Tris	VWR	JT4109-2
Triton X-100	VWR	9410
Tween-20	VWR	9480
X-gal	Goldbio	X4281C
Xylenes	VWR	XX00555

Table S2. Primary and secondary antibodies used for immunofluorescence

Primary antibodies	Vendor	Catalog number	Dilution
NKX2.1 (rabbit IgG)	Abcam	ab76013	1:200
E-CADHERIN (mouseIgG2a)	BD Biosciences	610181	1:500
NKX2.2 (mouseIgG2b)	Developmental Studies Hybridoma Bank	74.5A5	1:20
OLIG2 (rabbit IgG)	Millipore Sigma	AB9610	1:2,000
NKX6.1 (mouseIgG1)	Developmental Studies Hybridoma Bank	F55A10	1:20
Phospho-histone H3 (rabbit IgG)	Millipore Sigma	06-570	1:1,000
Phospho-histone H3 (mouse IgG1)	Cell Signaling Technology	9706S	1:100
PDGFRα (rabbit IgG)	Cell Signaling Technology	3174S	1:100
Secondary antibodies	Vendor	Catalog number	Dilution
Alexa Fluor 488 (Goat anti-Rabbit IgG)	Thermo Fisher Scientific	A-11008	1:500
Alexa Fluor 555 (Goat anti-Mouse IgG2b)		A-21147	
Alexa Fluor 488 (Goat anti-Mouse IgG2a)		A-21131	
Alexa Fluor 555- (Goat anti-Rabbit IgG)		A-21428	
Alexa Fluor 488 (Goat anti-Mouse IgG1)		A-21121	
Alexa Fluor 555 (Goat anti-Mouse IgG2a)		A-21137	
Alexa Fluor 647 (Goat anti-Mouse IgG1)		A-21240	

Table S3. Western Blot antibodies

Primary antibodies	Vendor	Catalog number	Dilution
Gli1 (V812) (rabbit IgG)	Cell Signaling Technology	#2354	1:1,000
Vinculin (E1E9V) XP (rabbit IgG)	Cell Signaling Technology	#13901	1:1,000
Secondary antibodies	Vendor	Catalog number	Dilution
Peroxidase conjugated AffiniPure F(ab)2 Fragment Donkey Anti- Rabbit IgG	Jackson ImmunoResearch	711-036-152	1:10,000

Table S4. qRT-PCR Primers

Gene	Sequence	Source
Gli1-F	GTGCACGTTTGAAGGCTGTC	(Han et al., 2017)
Gli1-R	GAGTGGGTCCGATTCTGGTG	
Gapdh-F	GGTGAAGGTCGGTGTGAACG	(Lewandowski et al., 2015)
Gapdh-R	CTCGCTCCTGGAAGATGGTG	

Supplementary Information References

Allen, B. L., Song, J. Y., Izzi, L., Althaus, I. W., Kang, J. S., Charron, F., Krauss, R. S. and McMahon, A. P. (2011). Overlapping roles and collective requirement for the coreceptors GAS1, CDO, and BOC in SHH pathway function. *Dev Cell* **20**, 775-787.

Han, Y., Xiong, Y., Shi, X., Wu, J., Zhao, Y. and Jiang, J. (2017). Regulation of Gli ciliary localization and Hedgehog signaling by the PY-NLS/karyopherin-beta2 nuclear import system. *PLoS Biol* **15**, e2002063.

Lewandowski, J. P., Du, F., Zhang, S., Powell, M. B., Falkenstein, K. N., Ji, H. and Vokes, S. A. (2015). Spatiotemporal regulation of GLI target genes in the mammalian limb bud. *Dev Biol* **406**, 92-103.